Dynamic Response of a Flexible Cylinder in Cross Flow Undergoing Vortex-Induced Vibrations (VIV)

By

Bianca Rachel Bitere

(Under the Direction of R. Benjamin Davis)

Abstract

This thesis experimentally investigates the vortex-induced vibrations (VIV) of a flexible cylinder mounted horizontally in uniform cross-flow with fixed-fixed boundary conditions. All experiments are conducted in a high-speed water tunnel. A spring steel beam is embedded within the silicone cylinder, promoting a response primarily in the cross-flow direction. The test article has an aspect ratio equal to 31.02, a mass ratio of approximately 1.6, and is tested with Reynolds number ranging from 2,850 to 19,000. Particular emphasis is placed on investigating the dynamic response at vortex shedding frequencies beyond the cylinder's fundamental natural frequency. Excitation pertaining to key lock-in events, intermittent amplitude switching, and multi-frequency contributions is studied. Finally, the influence of hysteresis on the lock-in duration and higher-order harmonics is discussed.

Index Words: vortex-induced vibrations, lock-in, flexible cylinder, hysteresis, multi-frequency excitation, higher order harmonics

Dynamic Response of a Flexible Cylinder in Cross Flow Undergoing Vortex-Induced Vibrations (VIV)

By

Bianca Rachel Bitere

B.S.M.E., The University of Georgia, 2019

A Thesis Submitted to the Graduate Faculty
of The University of Georgia in Partial Fulfillment
of
the Requirements for the Degree

Masters of Science

Athens, Georgia

2020

Dynamic Response of a Flexible Cylinder in Cross Flow Undergoing Vortex-Induced Vibrations (VIV)

By

Bianca Rachel Bitere

Major Professor: R. Benjamin Davis

Committee: Donald J. Leo
C. Brock Woodson

Electronic Version Approved:

Ron Walcott
Dean of the Graduate School
The University of Georgia
December 2020

Acknowledgments

This thesis was made possible with the support and guidance of many people.

It all starts and ends with my family. Thank you for always being a steadfast pillar of love and security throughout my academic journey. To my parents, you are my counsel, support, and role models. Alexandra and Andrei, thank you for the endless encouragement and laughter. Vă iubesc foarte mult! Doamne ajută!

To my research professor Dr. Davis, I cannot thank you enough for your immense patience, guidance, and respect. You have opened many doors of opportunity for me in the past, present, and future. For this, I am very grateful. I would also like to extend a sincere thanks to my fellow labmates. I have enjoyed learning and laughing alongside each of you. To Ryan, you will make an extraordinary professor one day. To George, I look forward to seeing where your determination and success takes you. Thanks for sharing the water tunnel.

My master's was made possible through the funding I received from the Science, Mathematics, and Research for Transformation (SMART) Fellowship established by the Department of Defense. Additionally, I would like to extend my gratitude to the faculty and staff of the college of engineering at the University of Georgia.

Lastly, I would like to dedicate this thesis in memory of Esther Parrish and Joe Johnson. Miss Esther, you were a wonderful English teacher and a pivotal force in my early education. Mr. Joe, your encouragement and wisdom laid the foundation to the start of my engineering career. May their memory be eternal.

Contents

List of Figures

List of Tables

Nomenclature

Acronyms

CF	Cross-Flow
DFT	Discrete Fourier Transform
DOF	Degrees of Freedom
FC	Flexible Cylinder
FSI	Fluid Structure Interaction
IL	In-Line
RMS	Root Mean Squared
VIV	Vortex Induced Vibrations

Symbols

A_{fc}	Cross Sectional Frontal Area of Cylinder
A_w	Cross Sectional Area of Test Section
D	Diameter
L	Cylinder Length
L_a	Active Length
U	Flow Speed
U_{ramp}	Ramping Velocity
ν	Fluid Kinematic Viscosity
ρ	Fluid Density

f_f	Forcing Frequency
f_n	Fundamental Frequency
f_{vs}	Vortex Shedding Frequency
m	Structural Mass
m_a	Added Mass
t	Time
t_{ramp}	Ramping Duration

Dimensionless Parameters

AR	Aspect Ratio
A^*	Reduced Amplitude
A^*_{RMS}	Reduced RMS Amplitude
A^*_f	Reduced Frequency Amplitude
B	Blockage Ratio
Re	Reynolds Number
S_c	Scruton Number
St	Strouhal Number
Ur	Reduced Velocity
ζ	Damping Ratio
f^*	Reduced Frequency
m^*	Mass Ratio

Chapter 1

Introduction

As the world population faces continuous growth, the demand for additional energy follows. Thus, the petroleum and gas industries face a parallel push to increase production by moving into deeper waters. Ocean risers play a crucial role in conveying crude oil and natural gas. Since risers are characterized by a large aspect ratio and low mass ratio, the exposure to ocean current can result in vortex-induced vibrations (VIV). VIV refers to the complex dynamic response of a bluff body when its wake pattern and structural vibrations are coupled. Vortex shedding induces lift and drag forces on the body. Lift forces usually induce cross-flow (CF) oscillations, while drag forces can induce in-line (IL) vibrations. Oscillations in the lift and drag direction will in turn change the vortex shedding characteristics of the flow profile. A number of engineering applications such as offshore risers, towed cables, mooring lines, bridges, and heat exchangers, are prone to vortex-induced vibrations (VIV).

An ocean riser is commonly characterized as having a low mass ratio (m^*) and high aspect ratio (AR). VIV can cause such slender bodies to oscillate at large amplitudes leading to accelerated fatigue failure [4]. Damage to ocean risers and pipes can cause substantial resource loss, serious economic impact on coastal activities, and immense environmental pollution. Such ramifications were evident in the sudden pipeline fatigue failure experienced

in the "Gannet Alpha" drilling platform in 2011; causing 21.6 billion tons of crude oil leaked into the North Sea [5, 6]. Unsurprisingly, the dynamic response of ocean risers undergoing VIV has received enormous attention in the past years from marine, civil, and mechanical engineers. However, there is still more to be discovered by probing different design topologies and configurations.

1.1 Overview

Over the past two decades, numerous numerical and experimental studies have been conducted to provide further insight on the dynamics of flexible cylinders undergoing VIV. Many conclusions have been made by changing the configurations of riser test articles. Such alterations include changing the tension [7, 8], suspending the cylinder at a curve or incline angle [9–11], using shear flow instead of cross flow [11,12], or varying the surface geometry [13] and roughness [14] of the cylinder. Understanding the hydrodynamic forces that drive such nonlinear responses is imperative to accurately predict and account for the possible failure of many engineering systems due to VIV.

The purpose of this study is to experimentally measure the dynamic response induced by VIV for a flexible cylinder in uniform cross flow. The test article is a silicone cylinder with an embedded thin spring steel beam. Similar cylinders have been considered in other VIV-based experiments, (e.g., Zimmer [15], who molded silicone around a metal beam to achieve a favorable tuning between the in-line and cross-flow natural frequencies). The test article used herein is unlike those from other studies because the design intent is to limit excitation to only the transverse, or cross-flow (CF), direction. The test article is placed in uniform cross-flow with fixed-fixed boundary conditions in a high speed water tunnel. The beam is oriented edge-wise to the flow such that it is weak in the CF direction and strong

in the streamwise, or in-line (IL), direction. Therefore, the response is predominately in the CF direction, and is measured in this direction only.

The test article has an aspect ratio equal to 31.02 and a mass ratio of roughly 1.6. The mass ratio in this study matches well with those typical for ocean risers, which tend to be below 3. However, the aspect ratio of the test article is comparatively lower than those typical for risers. Numerous studies have modeled ocean risers as flexible cylinders with both high [13, 16, 17] and low [7, 18, 19] aspect ratios (Ref. Table 2.2). These studies show that similar nonlinear VIV behavior is recorded for both cases. Therefore, the lower aspect ratio does not hinder the results of this study regarding comparisons with previous literature. The experiments are conducted over Reynolds numbers ranging from 2,850 to 19,000. The Reynolds number is intentionally kept at low orders of magnitude that are associated with horizontal ocean currents, as well as to compare with previous VIV publications.

Experimental areas of interest are as follows: capturing the dynamic response of the cylinder at vortex shedding frequencies beyond its first natural frequency; the ranges of flow speed corresponding to frequency lock-in; capturing the dynamic response due to the multi-mode excitation; documenting higher-order harmonics, and documenting the effects of hysteresis on the lock-in region and amplitude response. Therefore, the remainder of this thesis is organized as follows:

- **Chapter 2:** First, a general overview of vortex shedding, lock-in, and VIV is provided. This is followed by a literature review focusing on nonlinear dynamic response of flexible cylinders undergoing VIV in experimental applications.

- **Chapter 3:** The test article and water tunnel setup is provided in great detail. First, the design intent and manufacturing of the embedded flexible cylinder is explained. Then, the instrumentation and test section configuration are discussed.

- **Chapter 4:** This chapter explains the various water tunnel experimentation protocols used to capture the hydrodynamic response of the test article. A preliminary experiment collects the fundamental natural frequency and damping ratio of the cylinder in air and water. The second section discusses the primary experimentation methods.
- **Chapter 5:** Response data from the test are presented along with a thorough discussion of the results and implications.
- **Chapter 6:** Conclusions are presented along with other suggestions for further work.

1.2 Thesis Contributions

The primary contributions of this work are as follows:

- The design and manufacture of a novel VIV test article that includes an embedded internal structure such that vibration is limited excitation in the IL direction.
- The inclusion of thorough documentation related to the test article's construction and subsequent testing procedures.
- The design and manufacture of two new fixtures for the test section of the UGA water tunnel.
- The presentation and discussion of a rich data set exhibiting a number of complex VIV phenomena that are then discussed in detail.
- The use of a laser displacement sensor to collect the VIV response as opposed to the instrumentation employed in previous studies (shown in Table 2.2).
- The collection of response data during super-harmonic lock-in events, where the vortex shedding frequency synchronizes with an integer fraction multiple of the natural frequency.

- The observation of intermittent amplitude switching between the two lock-in cases where co-existing attractors are apparent.

Chapter 2

Background

Many numerical and experimental studies have been conducted to provide insight into a cylinder's response while undergoing VIV. However, the sensitivity of VIV to various parameters alludes easy generalizations. An overview of important VIV terminology and concepts is first provided. Then, a literature review focusing on the VIV of flexible cylinders is presented to summarize the experimental progress made in the past three decades.

2.1 Vortex-Induced Vibrations

VIV is a self-limiting, fluid-structure interaction phenomenon that occurs when both the structural dynamics of a bluff body, such as a cylinder, and its trailing wake are coupled. Many variables dictate the duration, magnitude, and likelihood of a body experiencing VIV [20–22]. Table 2.1 shows dimensionless parameters frequently used in conjunction with VIV studies. To ensure a foundational understanding of VIV, a review of the basics of vortex shedding, wake capturing, and the frequency lock-in are discussed in sequence.

Parameter	Symbol	Formula
Aspect Ratio	AR	$\frac{L}{D}$
Blockage Ratio	B	$\frac{A_{fc}}{A_w}$
Damping Ratio	ζ	$\frac{c}{2\sqrt{k(m+m_a)}}$
Mass Ratio	m^*	$\frac{4m}{\pi\rho D^2 L}$
Reynolds Number	Re	$\frac{UD}{\nu}$
Reduced Amplitude	A^*	$\frac{A}{D}$
Reduced Frequency	f^*	$\frac{f_f}{f_n}$
Reduced Frequency Amplitude	A_f^*	$\frac{Amp}{D}$
Reduced Velocity	U_r	$\frac{U}{f_n D}$
Scruton Number	S_c	$\pi^2 m^* \zeta$

Table 2.1. Dimensionless parameters

2.1.1 Vortex Shedding

Figure 2.1 shows the wake pattern development at different Reynolds numbers for a stationary cylinder placed in uniform flow [1]. When Re is between 40 and 300, flow separation causes the laminar development of vortex shedding. The vortices interact periodically to create a trailing vortex sheet in the wake. The rate at which the vortices shed off the body

is called the vortex shedding frequency (f_{vs}) and is given as

$$f_{vs} = \frac{StU}{D}, \tag{2.1}$$

where St is the dimensionless Strouhal number. The vortex shedding frequency is a reflection of the flow profile created by the body. Therefore, the dominant vortex shedding frequency is proportional to U while the Strouhal number, St, is largely constant ($St \simeq 0.18 - 0.2$) over a wide range of Reynolds numbers [22].

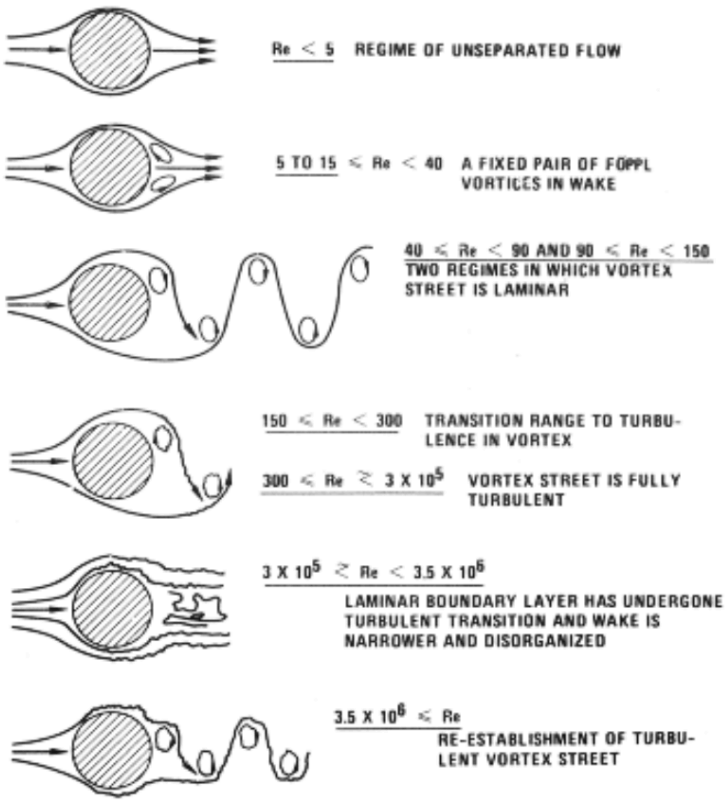

Figure 2.1. The development of flow separation and vortex shedding across a range of Reynolds numbers specifically for a smooth, stationary cylinder [1].

2.1.2 Lock-In

When an elastically restrained cylinder is subject to cross flow, the forces experienced by the body are often dominated by one or more discrete frequencies, denoted (f_f). The forcing frequency is almost always the vortex shedding frequency (f_{vs}). As the flow speed increases, f_{vs} increases. When f_{vs} approaches one of the cylinder's natural frequencies, f_n, the dominant forcing frequency can deviate from its nominal value of f_{vs} to match the cylinder's natural frequency [22]. When a body is excited at a natural frequency, it undergoes resonance. Typically, the dominant forcing frequency will remain equal to f_n for a range of flow speeds before returning to the nominal vortex shedding frequency. The phenomenon in which the vortex shedding frequency matches a body's natural frequency across a range of flow speeds is called *lock-in* or *wake capturing*.

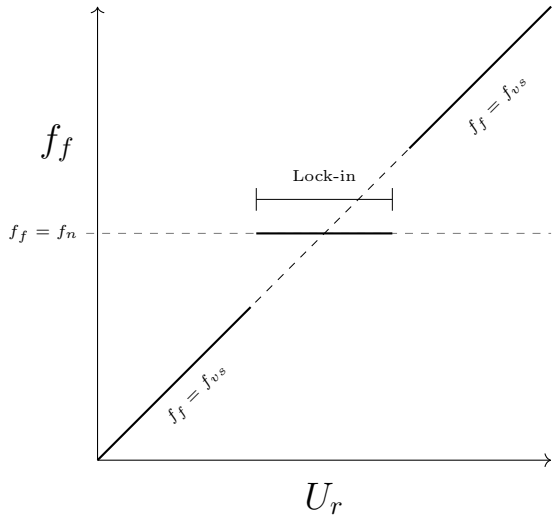

Figure 2.2. Schematic illustrating the lock-in phenomenon

Fig. 2.2 is a schematic illustration of lock-in. During lock-in, the vortex shedding frequency exhibits large deviations from the Strouhal line. Instead, f_{vs} is said to be controlled by the cylinder's (resonating) dynamic response. Certain changes in the cylinder's parameters can increase or decrease the frequency bandwidth in which lock-in is observed. The duration

of synchronization, or lock-in bandwidth, as measured by a range of reduced velocities, primarily depends on the structure's mass ratio (m^*) [23].

Commonly understood as the ratio between a cylinder's structural mass and the displaced fluid mass, the mass ratio is given by

$$m^* = \frac{4m}{\pi \rho D^2 L}, \tag{2.2}$$

where ρ is the density of the fluid. The variables m, D, and L correspond to the cylinder's physical characteristics. For a cylinder with a low mass ratio, the lock-in bandwidth is extended over a longer Ur range [20, 24]. An increase in lock-in bandwidth leads to longer exposure to large (possibly damaging) oscillations. Since ocean risers are characterized by a high aspect ratios and low mass ratio, lock-in bandwidth is important to their design because lock-in can lead to accelerated fatigue failure [25].

2.1.3 Branches of Synchronization

The development of the cylinder's excitation during lock-in is commonly classified by four response *branches*. The span of flow speeds where these branches are observed denotes the lock-in *bandwidth*. The lock-in branches are as follows: (i) initial, (ii) upper, (iii) lower branch, and (iv) desynchronization. Fig 2.3 shows a schematic of these branches versus reduced velocity [2].

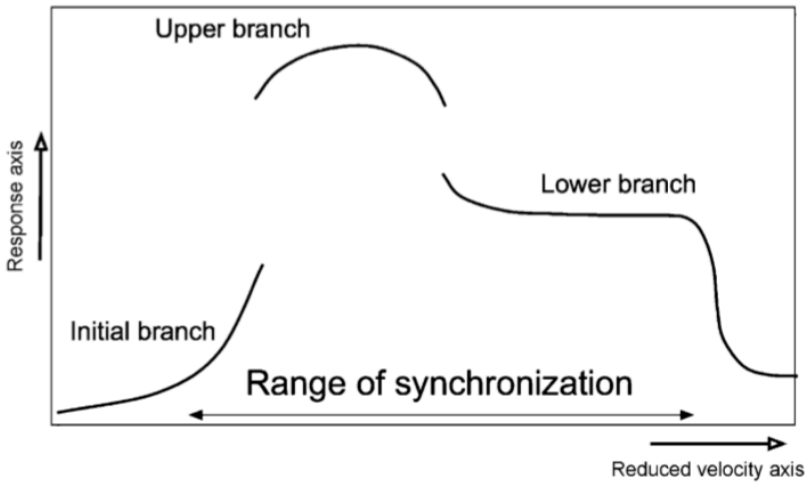

Figure 2.3. Sketch of the lock-in three-branch response model illustrated by Lucor *et al.* [2]

The initial branch corresponds to the situation in which the vortex shedding frequency (f_{vs}) is approaching one of the cylinder's natural frequencies (f_n). The upper branch occurs when the forcing frequency diverges from its nominal value of f_{vs} and begins attaching to f_n. Generally, the upper branch is categorized by large amplitude oscillations because structural resonance dominates the oscillations. The lower branch starts when the vortex shedding frequency begins to detach from the structural frequency. This is accompanied by a drop or decrease in amplitude because resonance has been disrupted. Lastly, desynchronization is where the coupling between the wake and cylinder's motion is completely interrupted, causing the amplitude to decay [2, 21, 22, 26].

The amplitude development across the lock-in bandwidth depends heavily on the mass-damping parameter ($m^*\zeta$) [23]. For low $m^*\zeta$, the initial, upper, and lower branches shown in Fig.2.3 are observed. With high $m^*\zeta$ values, only the initial and lower branches are evident in the response because true synchronization is not achieved.

2.2 Modeling Ocean Risers

Flexible cylinders with the same damping, mass, and mechanical characteristics in the in-line (IL) and cross-flow (CF) direction (e.g., risers, pipes, cables) can experience complicated dynamic response when undergoing VIV [27]. Two configurations are commonly used to model ocean risers: an elastically-mounted rigid cylinder and a flexible cylinder. Both models can be simplified as two degree-of-freedom (DOF) systems, allowing vibration in the CF and IL directions.

Elastically-mounted rigid cylinders have been extensively studied over the past several decades, but it was not until two decades ago that VIV research started modeling ocean risers as flexible cylinders. A notable difference between the elastically restrained rigid cylinders and flexible cylinders is that higher-order modes of the latter can be excited. When considering added mass ($m_a = {}^{\rho\pi D^2}/_4$) and hydrodynamic damping contributions, nonlinear behavior can manifest along the cylinder's length because of its elasticity [27]. This is evident by the introduction of competition among modes, a mixture of standing and traveling waves, and mono- or multi-frequency excitation [19]. For low Re environments, the VIV response of both models demonstrates a standing wave mode shape. In other words, the cylinders experience a single-mode lock-in. Unlike the elastically-mounted rigid cylinder, however, the flexible cylinder has the capacity to demonstrate a multi-mode response in higher Re cases [28].

In service, risers are subject to complicated flow conditions and exhibit equally complicated response. It is therefore an oversimplification to model a riser as an elastically-mounted rigid cylinder. The remaining review therefore focuses on flexible cylinders. Emphasis is placed on three major topics: multi-frequency excitation, higher order harmonics, and hysteresis. Table 2.2 summarizes a few of the experimental publications on flexible cylinders undergoing VIV.

Author	**Year**	**Model**	**Aspect Ratio**	**Mass Ratio**	**Flow Profile**	**Reynolds #**	**Instruments**
Trim *et al.*	2005	Riser & Stake	1400	1.6	Linearly Shear, Uniform	-	Accelerometers, strain gauges
Lie *et al.*	2006	Steel Riser*	3000	3.13	Linearly Shear	-	29 Biaxial gauges
Modarres-Sadeghi *et al.*	2008	3 FC	20.47, 27.88	-	Uniform Axial	-	Flow vis., optical motion-followers
Huera-Huerta *et al.*	2009	Vertical FC	94	3.13	Uniform	1200 to 12,000	Strain gauges
Lee *et al.*	2010	Vertical FC	58.58, 32.42	0.996	Linearly Shear	-	Accelerometer, bending-load cell
Song *et al.*	2011	FC	1750	1.0	Uniform	3,000 to 10,000	Fiber optic strain gauges
Sanaati *et al.*	2012	FC	165	low	Uniform	2,000 to 20,000	CDD camera, strain gauges, acceler.
Huera-Huerta *et al.*	2014	Vertical FC	158, 187	1.1, 2.7	Uniform	2,000 to 37,000	11 Strain gauges
Chen *et al.*	2015	FC Incline 25.3^o	144.7	high	Exponential Shear	1872.6 to 20,064	Accelerometer, hot-wire anemometry
Cen *et al.*	2016	FC	58	0.7,1.0,3.4	Uniform	800-13,000	Two high-speed cameras
Zhu *et al.*	2016	Curved FC	108	1.08	Shear	165 to 1129	High speed imaging, two cameras, dye
Han *et al.*	2017	FC Incline 45^o	350	1.9	Uniform	800 to 16,000	Strain gauges
Gao *et al.*	2017	FC	263	3.3	Uniform	9,230 to 54,500	88 Strain sensors
Gedikli *et al.*	2017	FC	41	3.76	Uniform	650-3,500	high-speed cameras
Gedikli *et al.*	2018	4 Embedded FC	41	1.1, 1.05, 1.02, 3.7	Uniform	650-5,500	high-speed cameras
Zhu *et al.*	2018	Curved FC	108	1	Exponential Shear	0 to 1,015	High speed cameras, dye
Aghazadeh *et al.*	2019	FC	73	1.2	Uniform	250 - 1525	Two high speed camera
Fan *et al.*	2019	FC	240	4.0	Uniform	250 -2300	Three high speed camera
Ma *et al.*	2020	Embedded FC	350	1.9	Uniform	800 -16,000	Strain gauges
Bitere	2021	Embedded FC	31	1.63	Uniform	2,000 to 19,000	Displacement Laser

Table 2.2. Experimental literature analysis of flexible cylinders undergoing VIV from the past two decades

2.2.1 Multi-Frequency Excitation

The IL response frequency is often twice that of the CF direction due to the rate of vortex shedding in the lift and drag direction [29]. Consequently, the dynamic response can exhibit different vibratory shapes in the IL and CF direction [27]. This is due to multi-frequency excitation, which refers to a combination of two or more significant frequencies driving the response of the cylinder [16].

Ocean risers are typically have aspect ratios of three or less. Cen *et al.* [19] experimentally investigated the effects of various mass ratios ($m^* = 0.7$, 1.0, and 3.4) on a flexible cylinder undergoing VIV. The test article with the lowest m^* produced the largest oscillation amplitude [19]. Modir *et al.* [30] also concluded that the peak VIV amplitude is inversely proportional to the mass ratio m^*. Cylinders with mass ratio $\simeq 1$ experience larger oscillation amplitudes in both the CF and IL directions.

Song *et al.* [16] conducted laboratory tests on a long flexible riser with an aspect ratio equal to 1750 using a wave basin. They observed responses up to the sixth resonance in the CF direction and up to the twelfth in the IL direction. Since higher IL modes are activated at a given flow speed, it is common for the amplitude response in the CF direction to be larger than in the IL.

2.2.1.1 VIV Response Asymmetry

A flexible body undergoing a multi-frequency VIV response will show spatially varying dominant frequencies [31]. If the difference in the primarily forcing frequencies is large enough, irregular oscillations may occur [21]. This is referred to as response *asymmetry* and can cause amplitude switching during excitation. Trim *et al.* [13] studied the difference in response of bare and covered helical straked riser in linear and sheared flow. It was observed that even in highly symmetric testing environments, a bare riser immersed in uniform flow

can show signs of response asymmetry. The nonlinear response switches from high to low amplitudes intermittently while subject to a constant flow speed.

Song *et al.* [16] also witnessed asymmetry in a bare riser subject to uniform flow. Their proposed reasoning for the response asymmetry involved the multi-frequency excitation with varying modal amplitudes, frequencies, and phase lags between the activated modes [16]. Response asymmetry has been observed in various other experimental configurations: a vertical flexible structure subject to uniform, shear, and step flows [13, 16, 27] and flexible cylinders inclined at a 45° yaw angle in uniform flow [10]. Accelerated fatigue damage in ocean risers can be caused when asymmetry is evident in both the CF and IL directions [16, 32].

2.2.2 Higher Order Harmonics

In VIV, it is not uncommon for a Fourier decomposition of the oscillatory response to exhibit higher harmonics at integer multiples of the dominant forcing frequency. In previous studies, higher-order harmonics have usually been observed during lock-in when the response amplitudes are highest [33, 34].

Higher-order harmonics are not evident in all VIV research focusing on flexible cylinders. For cases in which cylinder models are limited to CF excitation only, higher harmonics manifested more readily compared to cylinders with freedom in the IL and CF direction. Song *et al.* [16] and Vandiver *et al.* [33] found only the odd multiple harmonics in the CF response of a flexible cylinder. Cen *et al.* [19] identified contributions up to the sixth harmonic, observing both the odd and even multiples. Likewise, Ma *et al.* [17] documented up to the fifth harmonic when the response was locked-in to the second natural frequency in the CF direction.

Many parameters can influence the presence of higher harmonics in slender risers. An increase in the applied tension is known to inhibit the appearance of higher harmonics [17,35].

The presence of higher order harmonics suggests high amplitude nonlinear responses that are more likely to cause accelerated fatigue damage [16, 34].

2.2.3 Hysteresis

Another phenomenon commonly observed in VIV is *hysteresis*. Hysteresis is evident when a structure's response depends on whether the flow speed is increasing or decreasing. The parameters used to predict whether a flexible body will experience hysteresis varies in literature. For rigid cylinders, VIV-related hysteresis is said to be a function of the blockage ratio (B) and Re, specifically in cases where the blockage ratio is high and the Re is low. Prasanth *et al.* [36] discovered that hysteresis is primarily observed in the upper and lower lock-in branches for rigid cylinders. In addition, a cylinder constrained to only oscillate in the CF direction experiences larger hysteresis effects compared to a cylinder with two DOFs [36].

Gedikli *et al.* [18] focused on the hysteresis effects of a flexible cylinder undergoing VIV. Hysteresis was observed between the first and second modes in the CF direction. Hysteresis effect for a flexible cylinder is therefore found to manifest during the transition between resonances [18], rather than between the lower and upper lock-in branches, as in a rigid cylinder [36]. This is possibly due to the multi-frequency excitation that flexible cylinders can experience under VIV.

Chapter 3

Experimental Test Setup

The test article is designed with many constraints considered. The main limitations are ensuring the cylinder can undergo VIV excitation and fit the existing water tunnel test section. In this chapter, the fabrication of the embedded flexible cylinder is presented along with the specification of the associated instrumentation and test set up. Two additional fixtures are manufactured specifically to join the cylinder and water tunnel at the window interfaces. Their designs are presented as well. Lastly, the parameters of the final test article are provided.

3.1 Flexible Cylinder

Numerous cylinder configurations have been the focus of VIV research. To the author's knowledge, there has yet to be a publication considering the VIV effects of a flexible cylinder with an internally embedded beam that is designed to preference a given excitation. Here, the design an fabrication of the test article is discussed.

3.1.1 Materials

The test article is comprised of four materials: the encapsulation layer, substrate, spring steel beam, and two types of tape (lead and white vinyl). The encapsulation layer is made from pure silicone tubing (9.525 mm OD $\times$ 6.35 mm ID) with a uniform cross-sectional area and a 40A hardness rating. Roughly 0.5 m of silicone tubing is used to create the final test article. For the substrate, a soft shore 20A hardness cure liquid silicone mixture (Dragon Skin$^{\text{TM}}$ 20) is selected. The liquid silicone has a Young's modulus of 337.8 kPa and specific gravity of 1.08 g/cm^3. A spring steel beam ($\rho_s = 7700$ kg/m^3, $Y_s = 200$ GPa) is selected to comprise the embedded structure. The dimensions of the steel strip are 42.942 cm $\times$ 0.607 cm $\times$ 0.025 cm.

Two types of tape are used to coat the steel beam. The weighted lead tape (Maxfli) is meant to increase the total mass of the test article at its center. Three layers of lead tape are used. Each layer has the dimensions 9.906 cm $\times$ 1.06 cm $\times$ 0.0318 cm. The calculated density of the weighted tape, ρ_{lead} is approximately 655.74 kg/m^3. This is found by weighing an individual layer of lead tape and dividing by the calculated volume.

Lastly, the high performance vinyl tape (Prostripe) is used to provide a white-colored finish over the spring steel beam and lead tape. This is done to ensure a quality reading from the displacement laser (see Section 3.2). The vinyl tape is lightweight and provides no substantial weight to the overall assembly.

3.1.2 Cylinder Assembly

The first step in the cylinder assembly is preparing the spring steel beam. The desired beam dimensions are achieved by using a waterjet to cut out the strip of spring steel from a larger panel. The edges of the beam are then buffed to reduced sharpness. This prevents the beam from cutting into the silicone tubing during assembly later. Once the beam's dimensions

are recorded, white tape is used to indicate beam's the *active* length (ℓ_a); this refers to the cylinder's span that is exposed to the flow during experimentation.

Next, three layers of lead tape are wrapped around the midpoint of the beam, denoted ℓ_a. White vinyl tape is applied to coat the entire active length. Using a pen, the $\ell_a/2$, and $\ell_a/3$ span locations are lightly marked on the white beam. The markers act as a guide when positioning the displacement laser. Then, the finished steel beam is manually inserted into the encapsulation tubing.

The liquid silicone solution is mixed for two minutes and placed into a vacuum chamber to prevent porosity. Then, one end of the silicone tube is submerged inside the liquid substrate while the other is connected to a mini vacuum pump. Roughly 10V is supplied to the pump to create a large enough pressured difference between both ends, pulling the substrate through the interior and around the white beam. When the liquid silicone has encapsulated the entire beam, the pump is stopped. Binder clips are applied to each end, ensuring the liquid silicone does not leak during the solidification stage. The cylinder assembly is left to cure for over four hours and placed on a hot plate to speed up the solidification process. Once the cure time is complete, the test article is ready for the water tunnel test section.

3.1.3 Discrepancy

Figure 3.1 is an cross sectional illustration of the material layers at the cylinder's center. The lead tape covers the middle one-third of the cylinder's length. A consequence of this is that the material properties are not constant along the test article's length, and the cross sectional area of the test article ovals somewhat in the presence of the tape. A visual of the ovalling is shown in Fig. 3.2a. Fig. 3.2b compares the dimensional differences in locations with and without lead tape.

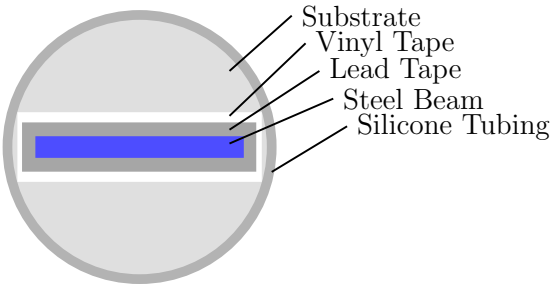

Figure 3.1. Schematic of the cylinder's cross-sectional area with material layers labeled.

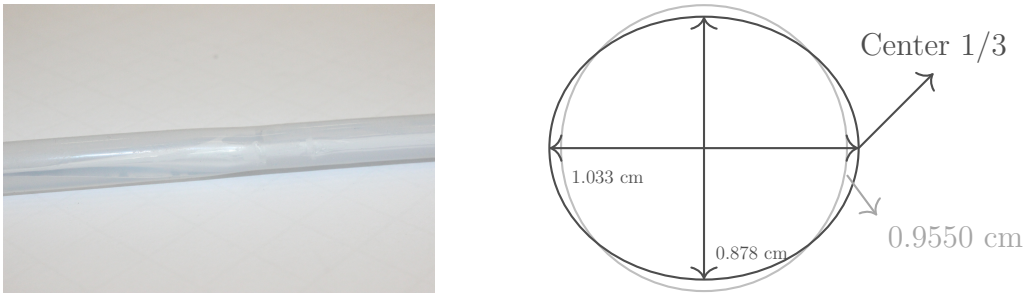

(a) (b)

Figure 3.2. (a) Photo of the area asymmetry at 1/3 span and (b) a diagram comparing the cylinder's cross sectional area at positions with (black) and without (gray) lead tape.

3.2 Instrumentation

A Micro-Epsilon optoNCDT 1420 (Fig. 3.3) is an laser optical displacement instrument and operates through the principle of optical triangulation to relay the location of a body. In this study, the displacement laser is used to collecting the cylinder's response at specific locations along the span. The light source wavelength is 670 nm, resulting in a visible red laser. The measuring range is 500 mm and resolution is equal to 2 μm. During experimentation, sampling rate is set to either 500 Hz or 4 kHz.

Figure 3.3. The Micro-Epsilon ILD optoNCDT 1420-500 laser

Color differences and mechanical vibration are two potential sources of error. The laser can experience undesirable alteration in its measurement when the target surface is comprised of many colors. From experience it is known that the laser works favorably with white colored surfaces; which is why the embedded beam is coated with white vinyl tape. To help alleviate instrument vibration, the laser is fixed in a 3D printed holster attached to a traverse (see Section3.4).

3.3 Water Tunnel Environment

3.3.1 Test Section

The high-speed water tunnel used in this study is located at the University of Georgia (UGA). For a detailed review on the water tunnel's capabilities and various applications, see Ref. [3].

The inner dimensions of the test section are $0.3 \times 0.3 \times 1\ m^3$. Fig. 3.4 provides a visual of the three types of windows used in the test section. The *breadboard* acrylic and aluminum *port* plate are selected to clamp either end of the test article and are installed on the sides on the test section. Two clear acrylic windows are used for the top and bottom openings. The transparency of the top window allows the displacement laser to shine through and onto the test article.

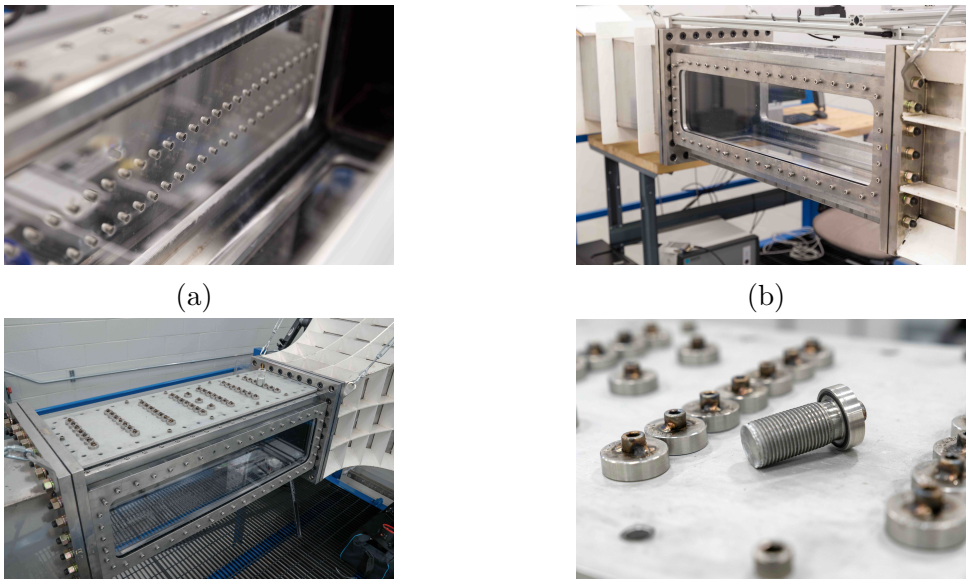

(a) (b) (c) (d)

Figure 3.4. Photographs of the (a) *breadboard*, (b) clear acrylic, and (c) aluminum *port* window with an closer look at the (d) aluminum window plugs. Images reproduced from Ref. [3].

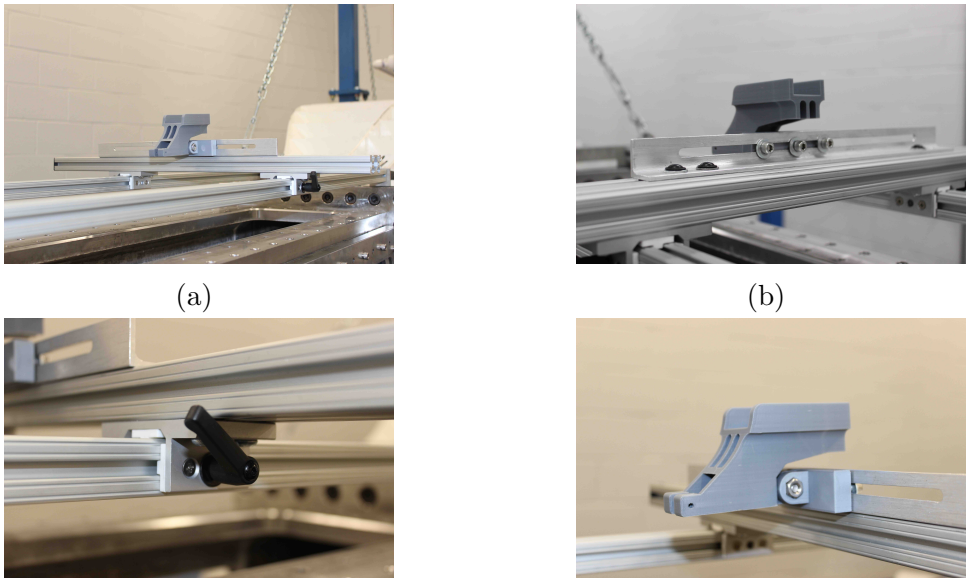

(a) (b) (c) (d)

Figure 3.5. Photos of the (a) front and (b) back of the traverse assembly, (c) friction arms, and (d) 3D printed laser holster.

A traverse is installed on top of the test section with the laser holster bolted to the railed carriage. By loosening the bolts and adjusting the holster, the laser is be continuously positioned along test section's width. Clasping the friction arms ensures the instrument is fixed during experimentation. Fig. 3.5 provides a photo of the traverse, laser holster, and friction arm.

3.3.2 Supporting Fixtures Design

Two fixtures are designed and manufactured to suspend the flexible cylinder across the test section, mimicking fixed boundary conditions. The clamps are not identical since both designs are a function of their mounting window. The fixtures are denoted as the *panel* and *plug*.

3.3.2.1 Panel

The panel is designed to fix the cylinder by pinching its end between the panel's back wall and *breadboard* window. This is done by screwing the panel into the interior *breadboard* wall. A Fortus 380mc Carbon Fiber machine is used to 3D print the panel.

(a) (b)

Figure 3.6. The (a) front and (b) back of the panel.

Fig. 3.6 provides photos of the panel fixture. The four angled holes along the corners allow the panel to be mounted to the interior wall of the *breadboard* window. The outer edges

are gradually angled and its thickness is kept minimal ($\simeq 0.762\ cm$ or 0.3") to minimize flow disturbance. The cylinder is strung through the panel's center and placed within the rounded groove on the back side. This allows the cylinder to be pinched in place while making sure the panel can be flush to the window.

3.3.2.2 Plug

The plug design is a combination of the existing port plug and the dye mount, previously shown in Fig. 3.4. The plug is designed to screw into the exterior aluminum wall until its end is flush with the interior. An inner hole of $\simeq 9.55mm$ is bored through the middle shaft, allowing the cylinder to be thread straight through. Additionally, the new plug design uses an O-ring to ensure the fit is waterproof.

(a) (b)

Figure 3.7. The plug (a) assembled with the flexible cylinder and (b) disassembled.

Fig. 3.7 provides the assembled and disassembled final plug design. The plug consists of a threaded cap and a rubber cork. An interior hole is drilled through the cork to match the flexible cylinder's outer diameter. The cylinder is then compressed into place, approximating a fixed boundary condition.

3.4 Final Assembly

During final assembly, an acrylic window is first installed to the bottom opening, followed by the side windows (*breadboard* acrylic and aluminum *port*). Then, mounting the test article to the side windows begins.

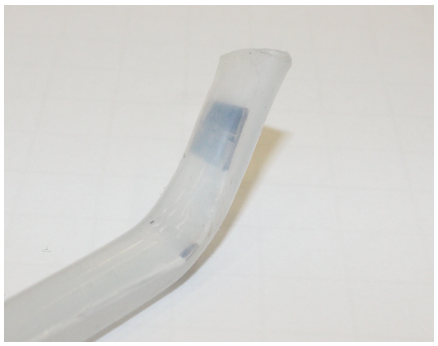

Figure 3.8. A photo of the bent cylinder's end.

First, the panel and cylinder are installed. For the test article to fit better inside the panel groove, a portion of the cylinder's end is manually bent. Fig. 3.8 provides a visual of the bent cylinder's end. This helps the threaded screws be installed into the panel. When the cylinder is fixed to the panel, a layer of electrical tape is wrapped around the cylinder's opposite end. Pulling the test article through the plug with the thick electrical tape ensures a tight fit that better approximates a fixed boundary. Once the cylinder is inserted though the plug, tension is applied, and the threaded cap is secured. This compresses the rubber cork, and keeps the cylinder horizontally taut across the test section width. A digital protractor is used to ensure the cylinder is level. Fig. 3.9 shows photos of the cylinder assembled in the individual fixtures, while Fig. 3.10 displays the test section with the cylinder installed. Again, both the panel and plug keep the cylinder fixed on either end of the test section.

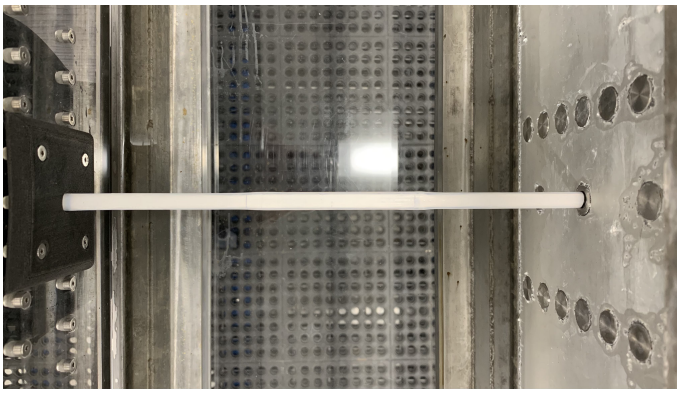

(a)

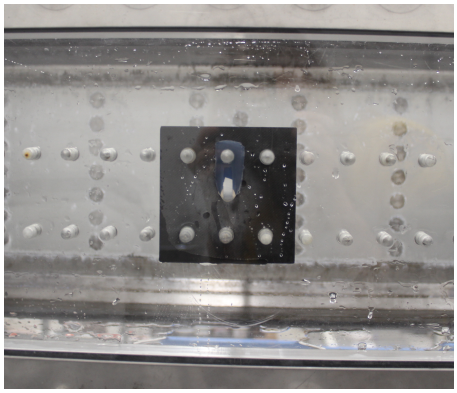

(b)

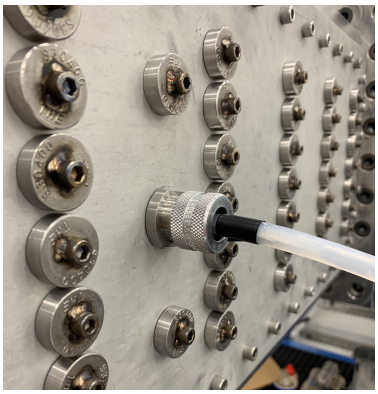

(c)

Figure 3.9. (a) Top-view of the test article fixed on both ends by the two fixtures. (b) The assembled panel and cylinder mounted to the *breadboard* acrylic window and (c) the assembled plug and cylinder installed into the aluminum *port* window.

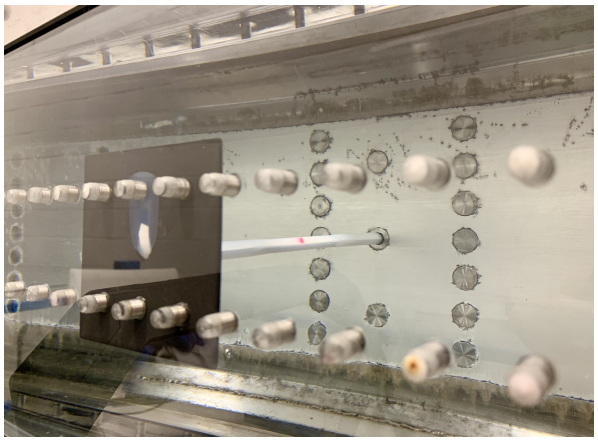

Figure 3.10. The flexible cylinder assembled to both fixtures submerged in inside the water tunnel environment.

Next, the clear acrylic window is bolted to the top of the test section. Then the traverse is attached and the displacement laser is inserted into the 3D holster. The laser is positioned onto the test article by manipulating the friction arms and positioning the holster along the double railing via the bolts. Lastly, the water tunnel is filled. Fig. 3.11 is a photo of the final experimental setup.

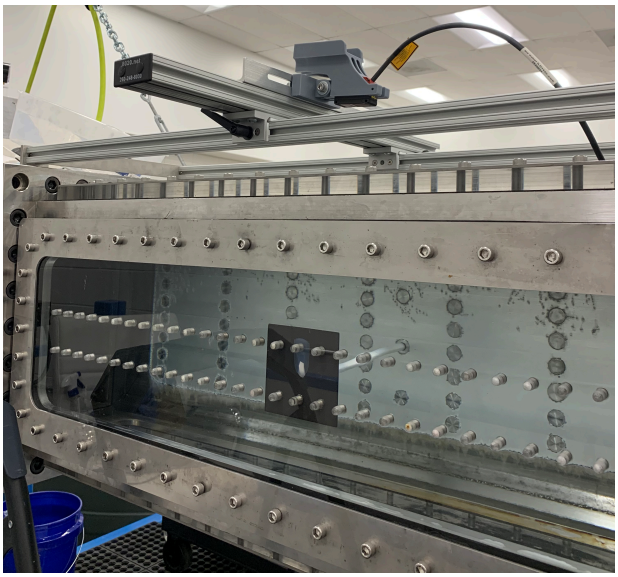

Figure 3.11. A photograph of the final assembly.

Before beginning experimentation, the cylinder's properties are documented in detail. There are notable discrepancy in the final assembly. The theoretical active length is calculated to be 29.718 cm by taking the test section width and subtracting by the panel thickness. However, the measured active length is 29.546 cm. This is a result of the panel not being mounted completely flush to the *breadboard* wall. The cylinder's thickness makes it very difficult to achieve the theoretical setup, which results in a minor off-set between the panel and wall of roughly 1.74 mm. Consequentially, the markers initially included on the beam assembly to indicate the fractional locations down the cylinder span are offset too. Table 3.2 provides the specific locations that the laser collected at and the naming convention based on the skewed marker span locations. The span notation is not perfect for the three locations;

however, the percent error does not exceed 2.1%. Therefore, the span notation is maintained throughout the rest of the thesis. Table 3.1 provides the final characteristics of the embedded flexible cylinder assembly. The active mass (m) is estimated by calculating the individual weight of each material within the measured L_a. From m, the mass ratio is calculated. All true locations are measured using the panel surface as the origin and a digital calipers.

Parameter	**Notation**	**Formula**	**Quantity**
Theoretical Length	L		29.718 cm
Active length	L_a		29.546 cm
Diameter	D		0.9525 cm
Active mass*	m		0.0342 kg
Added mass	m_a	$\pi\rho D^2 L_a/4$	0.021 kg
Fluid density	ρ		1250 kg/m^3
Aspect ratio	AR	L_a/D	31.02
Mass ratio	m^*	m/m_a	1.627
Blockage ratio	B	A_{fc}/A_w	3.13%
Scruton Number	S_c	$\pi^2 m^* \zeta$	0.583

Table 3.1. Final test article parameters

Span Notation	**Theoretical Location**	**True Location**	**Percent Error**
$1/2$	14.77 cm	15.08 cm	2.08%
$1/3$	9.85 cm	9.91 cm	0.582%
$2/11$	5.37 cm	5.40 cm	0.475%

Table 3.2. Final positioning of span locations during testing

Chapter 4

Experimental Procedure

This chapter provides an overview of the procedures followed during experimentation. Preliminary testing identifies the dry and wet natural frequencies and damping ratios of the test article. The remaining procedures focus on collecting the structure's response at various locations and flow condition. Since a single displacement laser is employed, the response at different span locations can not be collected simultaneously.

4.1 Preliminary Experimentation

This section discusses how the dry and wet fundamental frequency (f_n), and corresponding damping ratios (ζ) are calculated. While assembled inside the test section, the cylinder's free vibration response is obtained through a series of pluck tests in which an initial displacement is applied at the center. Once struck, the cylinder's response is recorded until the vibrations decay completely. The pluck test is performed for eight trials in air and water. For both media, the laser's sampling rate is set to 4 kHz and the laser is positioned to collect the response at one-third span (as measured from the panel end of the test article).

Once the time series is collected, it is processed to determine the frequency and damping. For both the dry and wet data, the damped natural frequency is easily identified from the frequency spectra and is nearly equal to the natural frequency because the levels of damping are low. The wet and dry damping ratio is determined by applying the logarithmic decrement method on the time series data. The log decrement equation can be given by

$$\zeta = \frac{ln\left(y_i/y_{i+n}\right)}{2\pi n}, \tag{4.1}$$

where y_i is the displacement of the i^{th} peak in the cycle and $y_i + n$ of the corresponding displacement of the $(i+n)^{th}$ cycle. For water, the selected i^{th} and $(i+n)^{th}$ peaks are five or six cycles apart. For air, the peaks are roughly ten cycles apart.

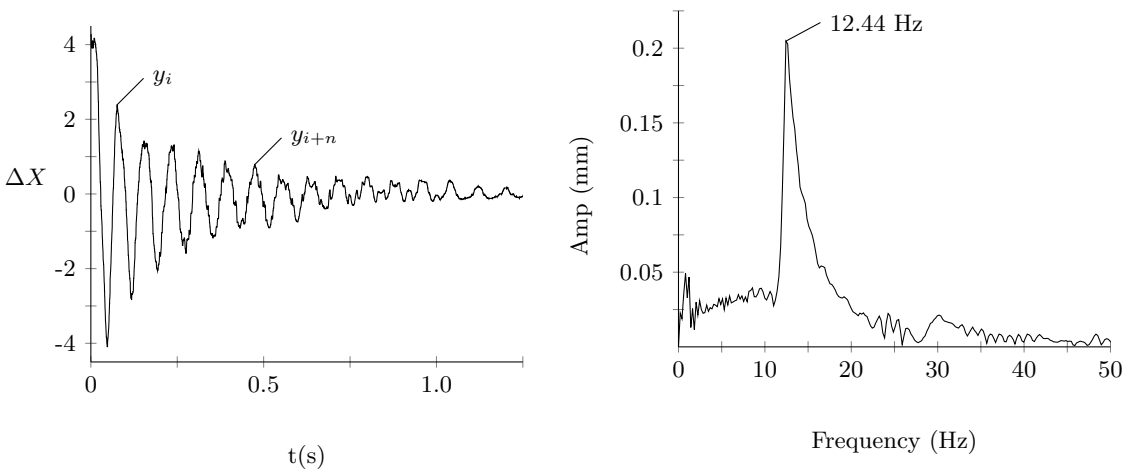

Figure 4.1. Time history and frequency spectrum of the transverse displacement collected at the test article mid-point during a wet free decay test.

Fig.4.1 shows an example of the cylinder's time history and frequency spectrum. The points used to calculate the damping ratio are labeled in the time history. The frequency with the highest amplitude peak is understood to be the first wet natural frequency and is also labeled.

Table 4.1 provides the average collected f_n and ζ for both the dry and wet case. It is expected that the test article's wet natural frequencies are lower than those in air. The inverse is true when comparing the damping ratio; ζ is higher in water than in air. The values in Table 4.1 are a mean of the eight total trails taken at the $^1/_3$ position for the two media, while Table 4.2 provides the resulting standard deviation (σ) between the recollected trials.

Medium	**1st Nat. Frequency (f_n)**	**Damping Ratio (ζ)**
Dry	15.9 Hz	0.0265
Wet	12.4 Hz	0.0363

Table 4.1. Dry and wet natural frequencies and damping ratios

Medium	**σ of f_n (σ_f)**	**σ of ζ (σ_d)**
Dry	0.099	0.0025
Wet	1.9 e-15	0.005

Table 4.2. Standard deviation (σ) for the dry and wet parameters provided in Table 4.1

4.2 Steady Flow Conditions

The first experimental condition involves measuring the cylinder's response at points along its span points under various steady flow speeds. The response is collected for 10 secs with the laser's sampling rate set to 4 kHz. A total of 22 flow cases are considered. The flow speed ranges from 0.3 to 1.35 m/s with increments of 0.05 m/s. The corresponding Reynolds numbers range from roughly 2,800 to 13,000. Table 4.3 displays the flow speed, reduced velocity, and Reynolds number pertaining to all 22 steady flow cases.

Flow Cases $[C]$	**Flow Speed (m/s)** $[U]$	**Reduced Velocity** $[U_r]$	**Reynolds Number** $[Re]$
C1	0.30	2.53	2851
C2	0.35	2.95	3326
C3	0.40	3.38	3801
C4	0.45	3.80	4276
C5	0.50	4.22	4752
C6	0.55	4.64	5227
C7	0.60	5.06	5702
C8	0.65	5.49	6177
C9	0.70	5.91	6652
C10	0.75	6.33	7127
C11	0.80	6.75	7603
C12	0.85	7.18	8078
C13	0.90	7.60	8553
C14	0.95	8.02	9028
C15	1.00	8.44	9503
C16	1.05	8.86	9978
C17	1.10	9.29	10453
C18	1.15	9.71	10929
C19	1.20	10.13	11404
C20	1.25	10.55	11879
C21	1.30	10.97	12354
C22	1.35	11.40	12829

Table 4.3. Flow cases for the steady flow experiment with corresponding dimensionless parameters.

4.2.1 Intermittent Switching

After collecting and reviewing the steady flow data, it became apparent that there exists a limited range of flow speeds where intermittent switching in the cylinder's response is observed. The dynamics involved in the intermittent switching regime are discussed in further detail Chapter 5.

To gain a better understanding of the switching phenomenon, the response data are collected for five minutes at both span locations. The laser's sampling frequency is lowered to 500 Hz for these tests. Additionally, a smaller increment of 0.025 m/s is used between flow speeds.

At both locations along the span, the switching becomes apparent when $U_r \approx 8$. The response is collected up to 1.05 $^m/_s$ at the $^1/_3$ marker and to 1.225 $^m/_s$ at the mid-point. Table 4.4 provides an outline of the flow cases, span location, and dimensionless parameters for the switching collection procedure.

Location	**Flow Cases** $[C]$	**Flow Speed (m/s)** $[U]$	**Reduced Velocity** $[U_r]$	**Reynolds Number** $[Re]$
$^1/_3$, $^1/_2$	C14	0.95	8.019	9028
$^1/_3$, $^1/_2$	C14A	0.975	8.230	9266
$^1/_3$, $^1/_2$	C15	1.00	8.441	9503
$^1/_3$, $^1/_2$	C15A	1.025	8.653	9741
$^1/_3$, $^1/_2$	C16	1.05	8.864	9978
$^1/_2$	C16A	1.075	9.075	10216
$^1/_2$	C17	1.10	9.286	10453
$^1/_2$	C17A	1.125	9.497	10691
$^1/_2$	C18	1.15	9.708	10929
$^1/_2$	C18A	1.175	9.919	11166
$^1/_2$	C19	1.20	10.130	11404
$^1/_2$	C19A	1.225	10.341	11641

Table 4.4. Intermittent switching experimental flow cases and corresponding dimensionless parameters.

4.3 Ramping Conditions

The cylinder's response is collected ramping up from 0.3 to 1.4 m/s followed by ramping down back to 0.3 m/s. The ramping duration in both cases is approximately 6 minutes and 3 seconds (363 s) and the laser's sampling rate is set to 500 Hz. The response is located at three locations along the flexible cylinder's length: $^1/_2$, $^1/_3$, and $^2/_{11}$. For the new $^2/_{11}$ location, only the ramping up is collected. Permanent deformation of the test section prohibited collecting reliable ramping down data at the $^2/_{11}$ location. Since the collection location for the $^2/_{11}$ condition is much closer to the fixed-end, the laser is more reliable at higher flow speeds. Therefore, the flow speed range for the ramping up at the $^2/_{11}$ location is 0.3 to 2 (m/s), which corresponds to reduced velocities ranging from 2.53 to 16.88. Table

4.5 specifies the parameters and conditions used curing ramp testing. The ramping duration and velocity are denoted as t_{ramp} and U_{ramp}.

Location	U (m/s)	U_r	Re	Direction	t_{ramp}	U_{ramp} ($^{mm}/_{s}$)
$^{1}/_{2}$	0.3 - 1.4	2.53 - 11.818	2,851 - 13,304	*Up, Down*	363	3.03
$^{1}/_{3}$	0.3 - 1.4	2.53 - 11.818	2,851 - 13,304	*Up, Down*	363	3.03
$^{2}/_{11}$	0.3 - 2.0	2.53 - 16.883	2,851 - 19,006	*Up*	374	4.5

Table 4.5. Ramping experimental procedure parameters.

The raw data from the ramping protocol undergoes corrective post-processing. This is because sometimes during the long duration test, the laser slips off the test article, especially when testing at high flow speeds. After the raw ramping data are collected, it is processed through a MATLAB code designed to remove the occasional slippage discrepancies in the data. This is done by establishing a threshold value for bad data points ($-35mm$). Any data points below the threshold are removed and replaced with the linear interpolation between the data points adjacent to the removed point.

Chapter 5

Results and Discussion

In this chapter, the experimental procedures detailed in Chapter 4 will be used to investigate the dynamic response of a flexible cylinder subject to VIV. A discussion of the notable VIV phenomena will be presented, including: lock-in, asymmetry, higher harmonics, and hysteresis. The initial lock-in is observed at the first natural frequency, and additional lock-in regions are evident at integer fraction multiples of the first natural frequency. This is presumed to be evidence of a super-harmonic resonance where the vortex shedding frequency synchronizes with a harmonic component of the structure's nonlinear oscillation.

Since the mass ratio ($m^* = 1.63$), aspect ratio ($AR = 31$), and damping ratio ($\zeta = 0.0363$) are the same in all experiments, comparisons will be drawn from the cylinder's amplitude response across a reduced velocity (U_r) range, and at different locations along the cylinder's span. A series of time histories are first presented to introduce the various types of VIV observed, followed by individual discussion of each type.

5.1 Time and Frequency Domain Data

As discussed in Section 4.2, the cylinder's transverse response is collected asynchronously at two span locations (1/2 and 1/3) across a discrete range of steady flow speeds. In Fig. 5.1, the normalized time history and corresponding frequency spectra collected at the 1/2 position are shown for select flow cases. These cases are chosen specifically to show qualitative changes in the cylinder's VIV behavior. The time histories are ordered as follows: before and during f_{n1} lock-in, during intermittent switching, and before and during the lock-in at $2f_{n1}$. The test cases are referred to as C4, C6, C17, C19, and C20, corresponding to flow speeds of 0.45, 0.55, 1.1, 1.2, and 1.25 m/s (see Table 4.3). The first column provides the amplitude normalized by the cylinder diameter, denoted A^*, for a 10 second collection window at a uniform flow, whereas the second column focuses on a narrower time interval from 4.5 to 5.5 seconds. In the third column, the amplitude spectra generated by the discrete Fourier transform (DFT) are shown. The amplitudes in the frequency spectra are also normalized by the cylinder diameter. Labels are provided to indicate the dominant frequencies.

Off-resonance oscillations with low amplitudes are evident for case C4 as shown in Fig. 5.1a. Here, the reduced velocity is $U_r \approx 3.8$, corresponding to a Reynolds number of approximately 4,300. The frequency spectrum indicates two dominant frequencies at 9.7 and 13.6 Hz, with the latter having a higher amplitude. Interestingly, these dominant frequencies are situated above and below the test article's fundamental frequency of 12.4 Hz. Assuming $St = 0.18$, the theoretical vortex shedding frequency for case C4 is 9.92 Hz. Because the response has significant content at both 9.7 and 13.6 Hz, the test article is said to experience multi-frequency excitation at this flow speed. Typically, flexible cylinders show only a single frequency response at low flow speeds; this occurrence of multiple dominant frequencies at lower U is likely due to the flexibility of the test article inducing dual vortex patterns in the wake.

As U_r increases to 4.46, a distinct increase in the response amplitude and the dominant frequency is observed. Here, the vortex shedding frequency is synchronized with the first natural frequency of the cylinder ($f_{n1} = 12.4$ Hz), evidenced by the single dominant frequency in spectrum. This phenomenon is known as frequency lock-in, and the high amplitudes are due to a resonance response resulting from the coincidence between the natural frequency of the structure and the vortex shedding frequency. Lock-in is often predicted when the the reduced velocity approaches $1/St$ [37]. Lock-in is discussed in greater detail in Section 5.2.1.

Beyond the first lock-in, there exists a range of flow speeds where the dynamic response intermittently switches between two distinct amplitudes. This is evident from the time histories corresponding to C17 ($U_r = 9.29$) and C19 ($U_r = 10.13$) in Figs. 5.1c and 5.1d. The sporadic amplitude switching is commonly referred to as response *asymmetry* and is well-documented for flexible cylinders [13, 16, 27]. A detailed analysis of asymmetry is provided in Section 5.3.

Fig. 5.1e shows the VIV response for C21 ($U_r = 10.97$). Here, the response is dominated by its component at 25 Hz, which is nearly two times the fundamental frequency of the test article. This response is presumed to represent a super-harmonic resonance, which tend to occur at frequencies that are integer multiples of a particular natural frequency. The phenomenon occurs when the vortex shedding frequency has locked-in to a higher-order harmonic of the cylinder's nonlinear oscillation.

In regard to a cylinder undergoing VIV, there seems to be a lack of research documenting the presence super-harmonic resonance. Super-harmonic resonance is more frequently seen in VIV studies where the structure has a non-circular cross-section.

Baek *et al.* [38] conducted a numerical analysis of super-harmonic excitation in the trailing wake created by a cylinder oscillating torsionally. However, Baek *et al.* was more successful in numerically tracking sub-harmonic resonance. While studying the effects of time-varying tension on a flexible cylinder, Ma *et al.* [17] observed several higher harmonic frequencies

when lock-in excites a mode in the cross-flow direction. The test article used in this experiment was comprised of an internal copper pipe wrapped by a silicone tube, which is similar in nature to the test article used in this study; however, super-harmonic resonance was not observed in the test.

The possibility that the response in Fig. 5.1e is not super-harmonic resonance but rather lock-in with the test article's second natural frequency is unlikely. Based on the natural frequencies of a clamped-clamped beam [1], the second natural frequency of the test article is expected to be near $2.75 * f_{n1} = 34$ Hz. Furthermore, the response of the second mode is not expected to be significant because the measurement location at one-half span coincides with the node of the second bending mode.

Overall, the time histories and spectra in Fig. 5.1 show the dominant frequency tends to increase with U_r. This is even observed within the asymmetric response regime and is in agreement with other studies [16, 19]. Similarly, the amplitude response also tends to increase with U_r. Across all trials involving steady flow conditions, the maximum amplitude is found to be about 0.6D and was measured when $U_r = 10.13$ (just below the onset of the lock-in at $f_f = 25$ Hz).

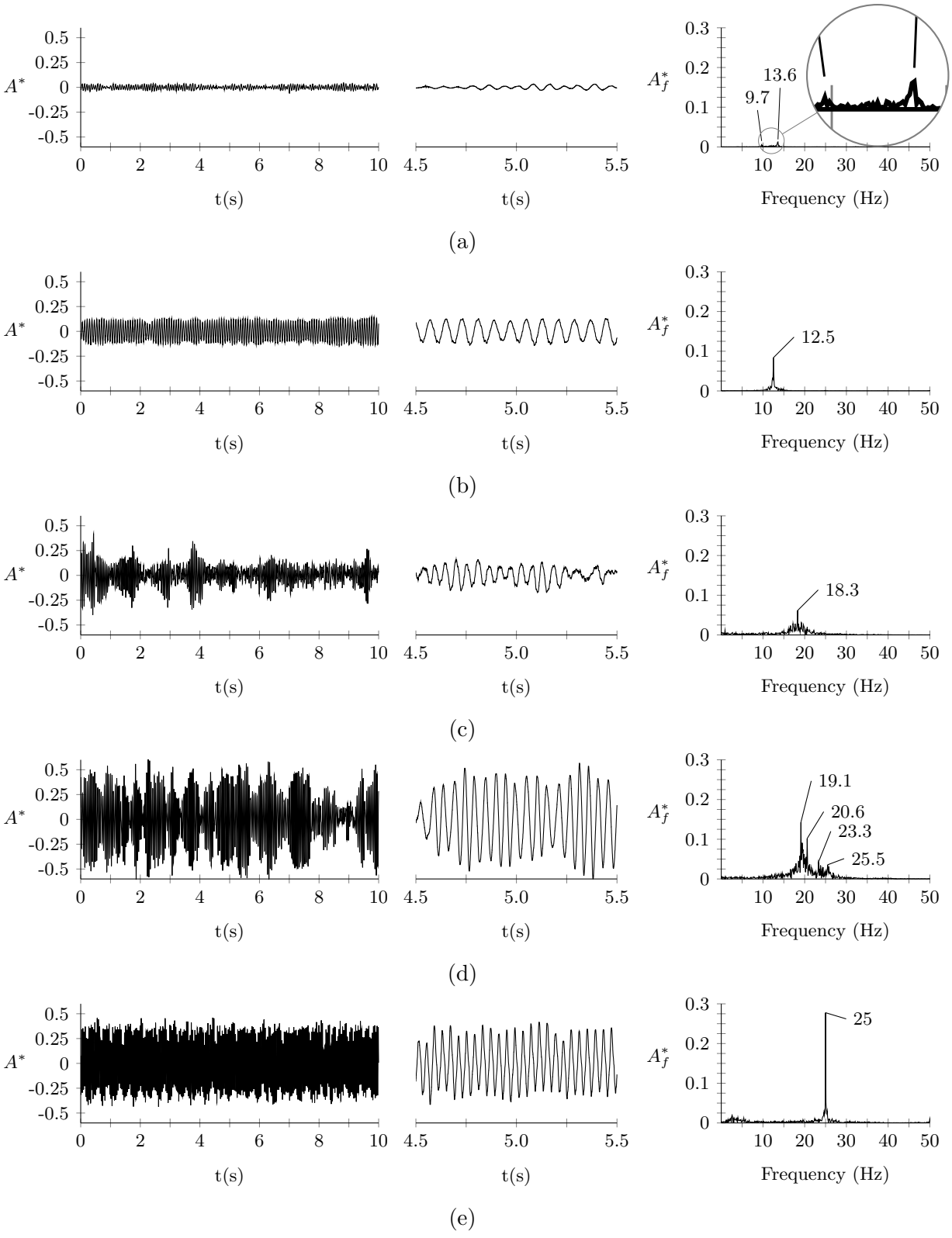

Figure 5.1. Time histories and frequency spectra at the ½ position for U_r equal to (a) 3.8, (b) 4.46, (c) 9.29, (d) 10.13, and (e) 10.97.

5.2 Lock-in and Multi-Frequency Excitation

Figs. 5.2a and 5.2b plot the frequency components that significantly contribute to the cylinder's response at each steady flow case (Section 4.2). The included frequencies are determined by applying the DFT to the response time histories. A significance factor is calculated based on the frequency component's contribution to the cylinder's root-mean squared (RMS) response amplitude. In Fig. 5.2, frequency components with amplitudes of more than 20% of $\sqrt{2}\times$ the RMS response are denoted with filled black dots, and frequency components with amplitudes between 5 and 20% are marked as hollow circles. The largest frequency components observed at each flow speed are outlined in red. The dashed horizontal lines at $f^* = 1$ and 2.75 indicate the first and second natural frequencies while the other horizontal lines are shown at select multiples of $f^* = 1$. The angled dashed line is the Strouhal line with $St = 0.18$. Fig. 5.3 shows the RMS response normalized by the diameter across the range of tested U_r values. The various VIV phenomena evident in Figs. 5.2 and 5.3 are discussed individually in the following subsections.

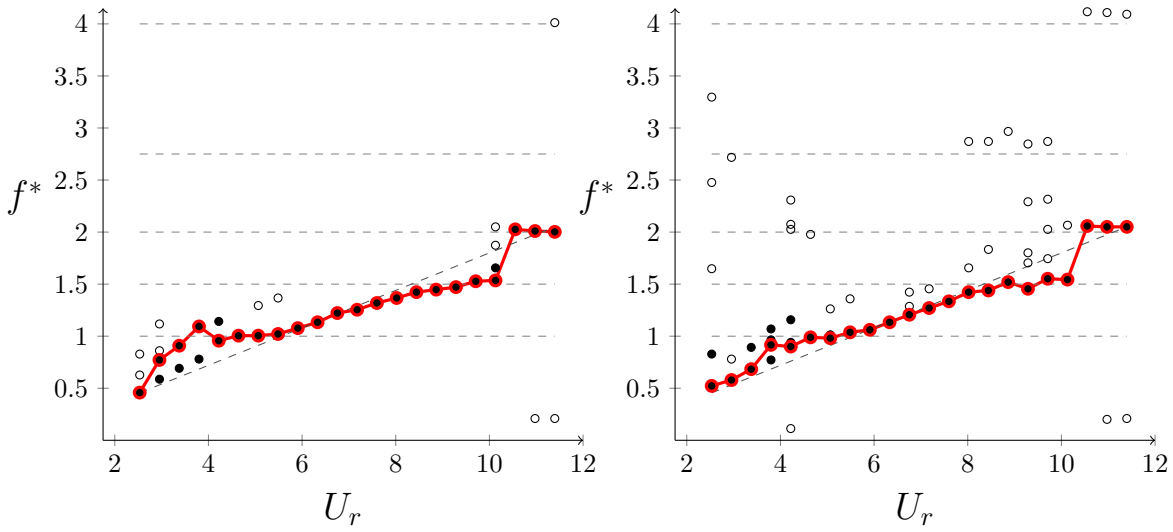

Figure 5.2. Significant components of the frequency spectra across a range of reduced velocities observed at the (a)1/2 and (b) 1/3 span locations.

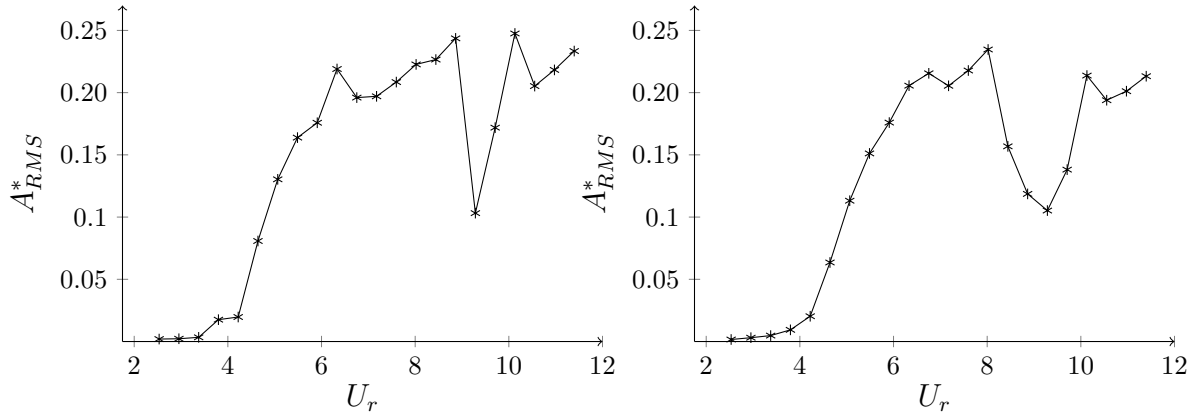

Figure 5.3. Normalized RMS response versus reduced velocity recorded at the (a)1/2 and (b) 1/3 span locations.

5.2.1 Lock-in

As previously discussed, the test article experiences lock-in multiple times during experimentation. The primary lock-in event occurs when the vortex-shedding frequency synchronizes with the first natural frequency. Synchronization begins at $U_r \approx 4$ and is more apparent in the data measured at 50% span. Additional lock-in events are seen at 3/2 and two times the fundamental frequency. In these cases, the vortex shedding frequency seems be be synchronizing with a higher-order harmonic of the test articles nonlinear oscillation to produce what is known as a super-harmonic resonance.

5.2.2 Multi-Frequency Excitation

First, consider the filled black dots in Fig. 5.2 which correspond to *major* frequencies with peak magnitudes that are greater than 20% of $\sqrt{2}\times$ the RMS response. At low flow speeds more than one major frequency drives the cylinder's response. At $U_r = 3.8$, two major frequencies are present at 50% span, whereas three dominate the response at 33% span.

Next, examine the population of hollow circles. They refer to the *minor* frequencies with a significance factor between 5-20%. The 1/3 position shows a greater number of minor frequencies. This can be explained by considering the first mode shape. Since the mid-point is near the anti-node, it will experience greater displacement during the first lock-in. In turn, the forcing frequencies closest to $f_{n1} = 12.4$ Hz will be more amplified in the response at half span. This causes the minor frequency to contribute relatively less; thus, they fail to surpass the 5% threshold and do not appear in Fig. 5.2a.

5.3 VIV Response Asymmetry

Here, the response asymmetry is considered. To better characterize this response, relatively long time histories were collected at 1/3 and 1/2 span. The 1/3 data were taken between $U_r = 8$ to 8.86 while the 1/2 data were taken from $U_r = 8$ to 10.34.

Figs. 5.4 and 5.5 provide the switching time history and spectrum analysis at a constant flow speed of 1.05 m/s for both the 1/3 and 1/2 locations. The first row consists of the response across a three minute time window. The second row isolates a portion of the lower amplitude while the third row isolates a higher amplitude response. Seven seconds of both the higher and lower responses are presented for the 33% span location. For the 50% position, an interval of six seconds is used. Figures in the far-right column are the amplitude spectra of the corresponding time histories. Distinct peaks in the spectra are labeled for clarity.

This switching phenomenon is due to the presence of co-existing *attractors*. The lower attactor has a reduced amplitude of about 0.1, while the reduced amplitudes reaches up to 0.4 in the other.

In Fig. 5.4f, the dominant frequency associated with the larger response at the 33% position is 18.14 Hz, which is approximately $1.5 * f_{n1}$. It is possible that the high-amplitude response shown in Figs.5.5e and 5.4e reflects sub-harmonic resonance at a integer fraction

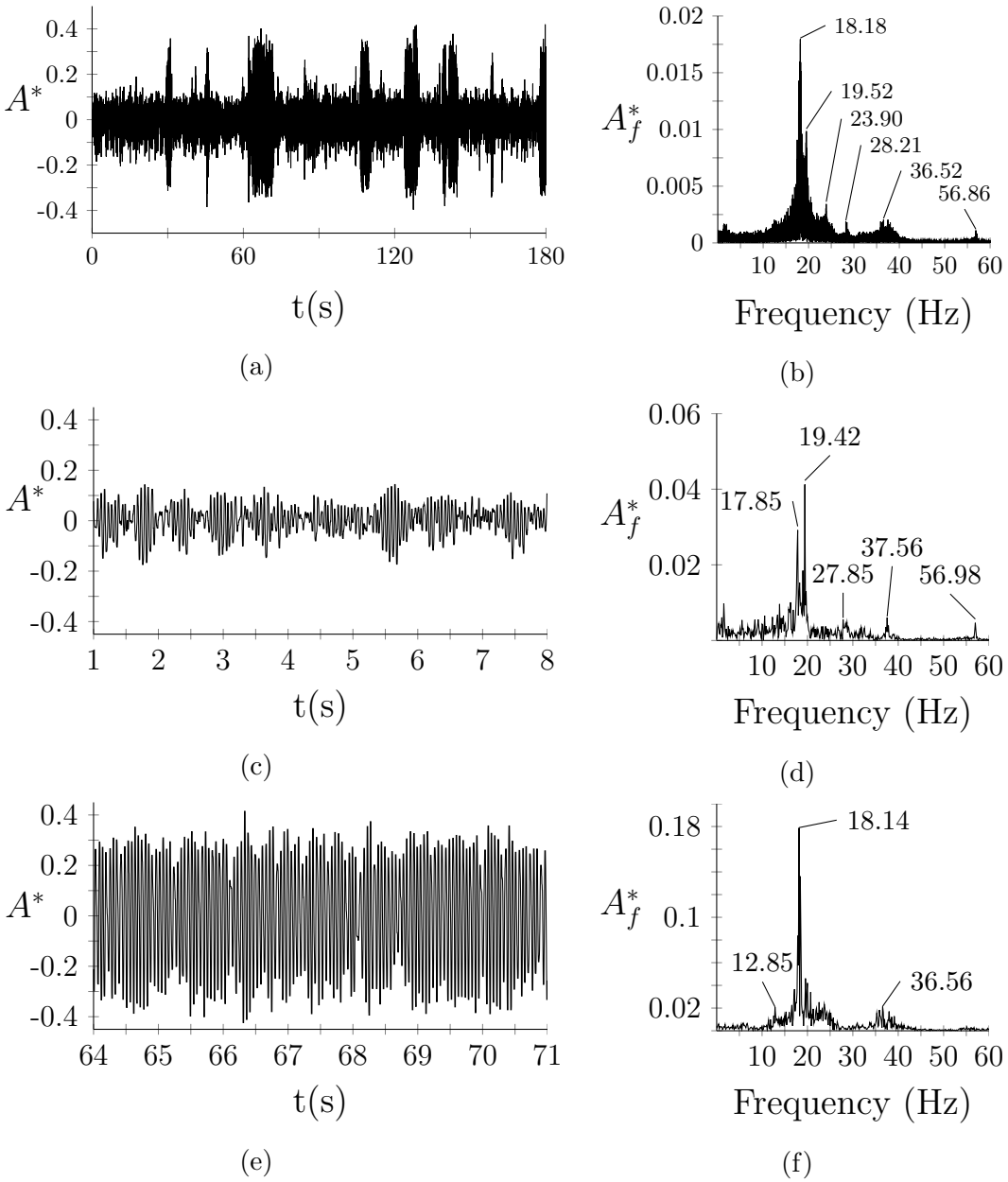

Figure 5.4. Time history and frequency spectrum showing asymmetric response. Data are collected at 1/3 position with a constant reduced velocity of 8.86.

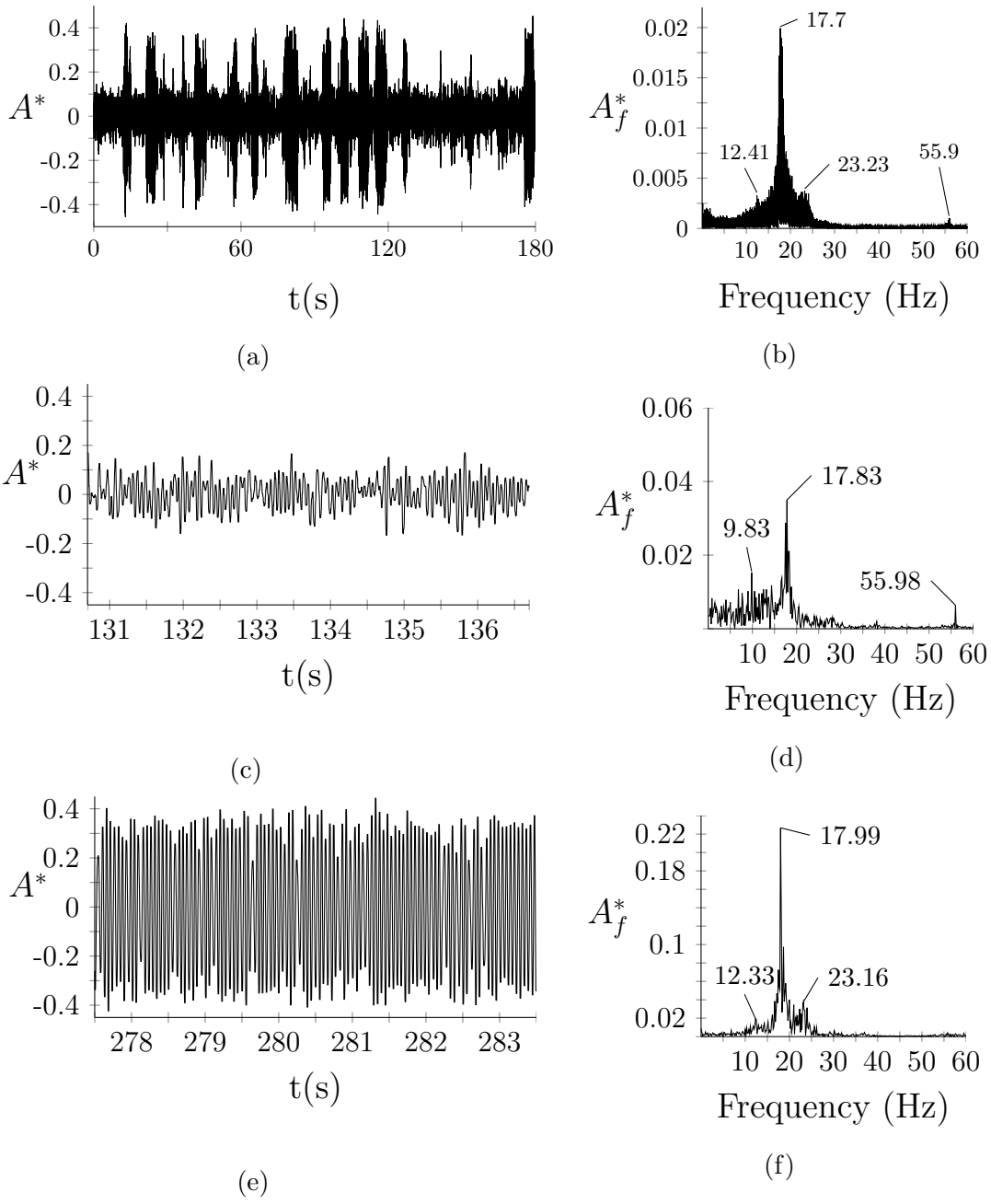

Figure 5.5. Time history and frequency spectrum showing asymmetric response. Data are collected at ½ position with a constant reduced velocity of 8.86.

of the fundamental frequency. Additional frequency components are observed at 12.85 and 36.56 Hz, which correspond to the first and second natural frequencies of the cylinder. The presence of these resonances suggest that the cylinder's excitation is somewhat broadband. As for the low amplitude responses, the two frequencies dominate the response—one at 17.85 Hz and the other at 19.42 Hz.

5.4 Higher Order Harmonics

Higher harmonic components are observed during the recorded lock-in events. The first lock-in occurs when the forcing frequency is near 12.4 Hz. Fig. 5.6 shows the response in the frequency domain at 0.55 m/s during the first lock-in.

At 50% span, the dominant frequency is 12.5 Hz, and its second, fourth, and fifth-order harmonic components appear as distinct peaks at 25, 50, and 62.5 Hz. The expected third harmonic should be equal to 37.5 Hz (i.e. 3×12.5); however, the third component is observed at 38.9 Hz and has a considerably smaller peak than the surrounding harmonics. This is possibly due to the presence of the second natural frequency. Since the 1/2 position is near the node of the second mode shape, frequency components close to 34.2 Hz will be attenuated. At 33% span, harmonics of the 12.3 Hz mode up to the seventh-order are apparent.

Fig. 5.7 shows the frequency spectra during the second lock-in event while dwelling at a constant flow speed of 1.3 m/s. The dominant forcing frequency at 50% span is located at $2f_{n1} \approx 25$ Hz. Indications of other higher harmonics are observed in the spectra and are integer multiples of 25 Hz. Up to the 8^{th}-order harmonic is evident. Similar content is apparent at the 1/3 position. Also, Fig. 5.7 shows a distinct peak near 2.5 Hz for both spanwise positions, which is one fifth of the fundamental frequency.

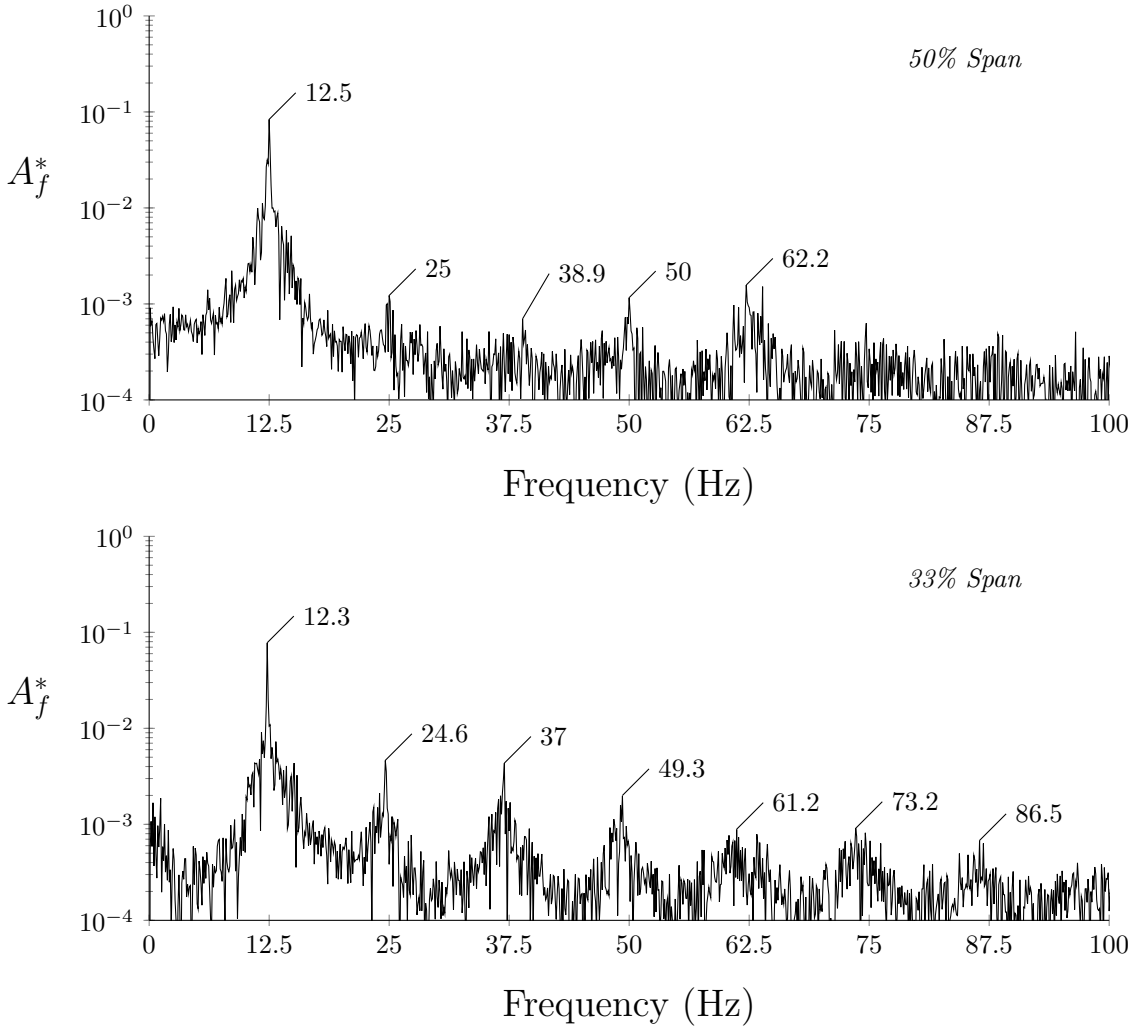

Figure 5.6. Frequency domain of the first lock-in response at a constant reduced velocity of 4.65 as measured at (top) 50% and (bottom) 33% span.

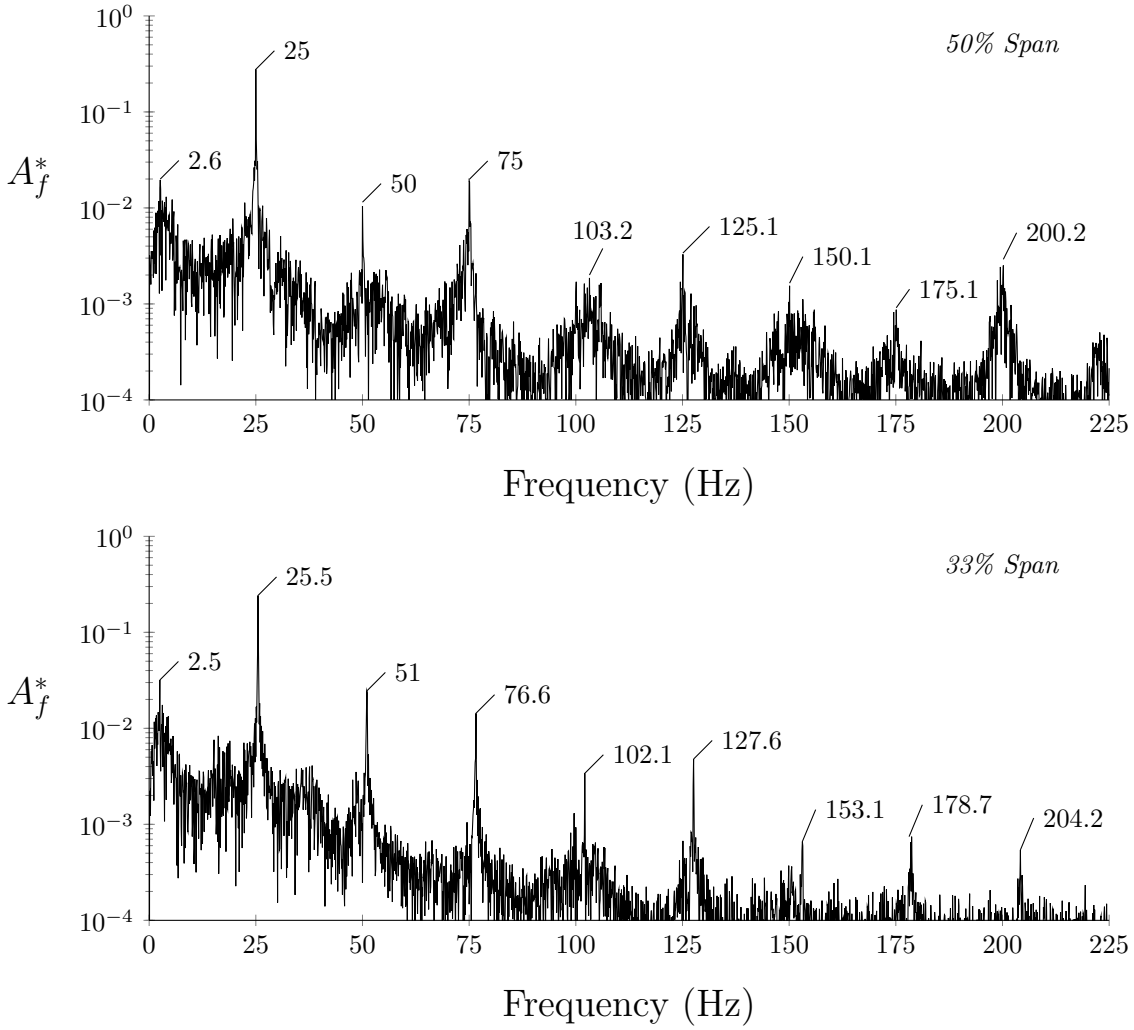

Figure 5.7. Amplitude spectra of the lock-in response at a constant reduced velocity of approximately 11 as measured at (top) 50% and (bottom) 33% span.

5.5 Hysteresis

Hysteresis is the phenomenon where a physical property varies inconsistently with respect to changes to its cause. For example, the vortex shedding frequency (the physical property) observed at a given flow speed often depends on whether the flow velocity (the cause) is increasing or decreasing. Data collected in Section 4.3 is used to investigate the effect of hysteresis in this study.

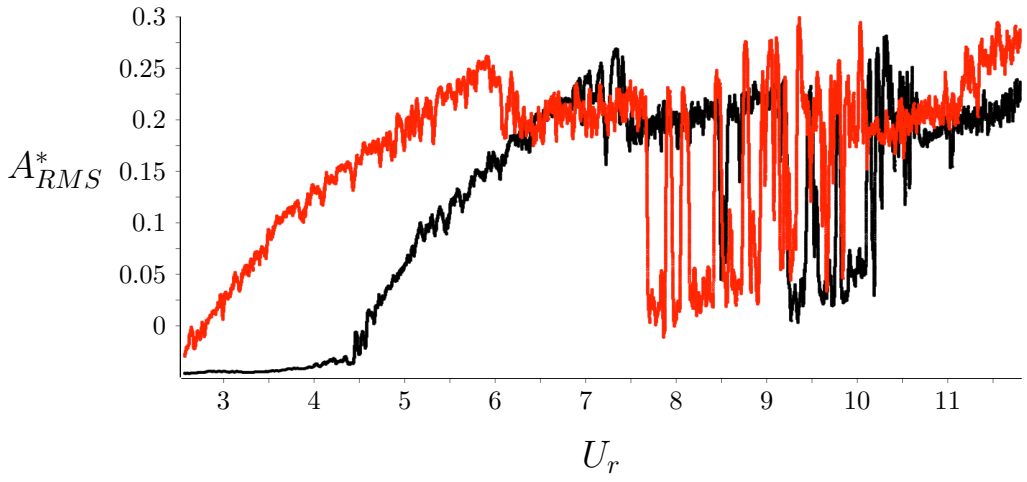

(a)

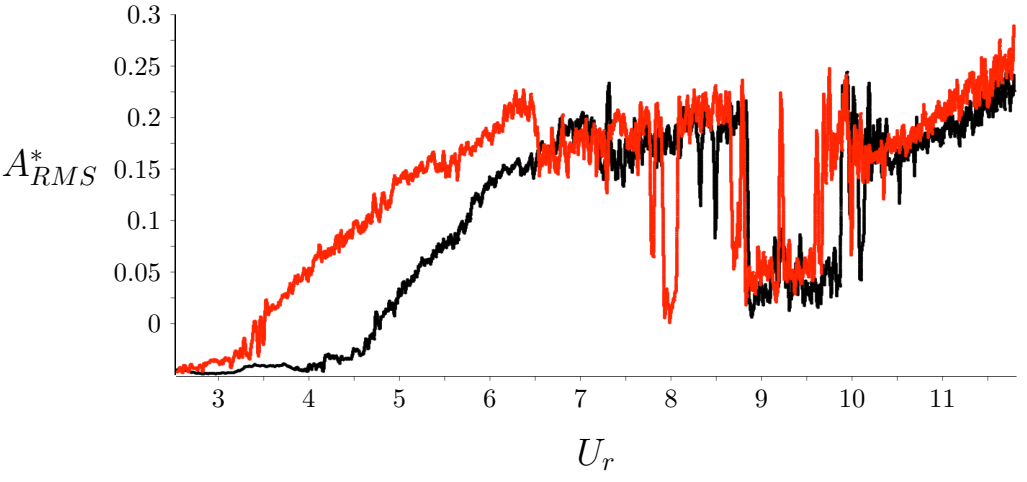

(b)

Figure 5.8. The A^*_{RMS} plotted when increasing (black) from 0.3 to 1.4 $^m/_s$ and decreasing (red) accordingly for the (a) 1/2 and (b) 1/3 span.

Fig. 5.8 plots the RMS of the reduced amplitude collected when ramping up and down between 0.3 and 1.4 m/s. For both ramps, the velocity rate remains constant at 0.00303 m/s^{-2}. The reduced RMS amplitude, $A^*_{textRMS}$, is obtained via a moving RMS with a window size of 500 data samples. Hysteresis is apparent at both span locations by the notable offset in the response amplitude between flow directions. Similar to hysteresis effects associated with rigid cylinders, Fig. 5.8 shows shifts in the lock-in response branches (i.e., initial, upper, and lower) that depend on whether the flow velocity is increasing or decreasing [36].

The response asymmetry regime also exhibits hysteresis. In Fig. 5.8a, asymmetric response exists across a wider flow regime when ramping down as opposed to up. This trend is also evident in the response taken at the 1/3-span location in Fig. 5.8b. The hysteresis effects observed in this study agree with the findings of Gedikli et al. [18].

Frequency domain analysis is also conducted by applying the DFT to the time history of the ramping experiments. Fig. 5.9 shows the spectrograms for both ramping cases collected at the 1/3-span location. The frequency contribution is plotted against reduced velocity, and the color gradient describes the normalized power spectral density (dB) of the frequency components. Notable VIV phenomena are labeled on both spectrograms using the corresponding abbreviations: (L) lock-in, (H) super/sub-harmonics, and (A) response asymmetry. The lock-in frequency bandwidth stretches across a wider range of flow speeds for the decreasing velocity rate as opposed to increasing, and this is evident for both the f_{n1} lock-in ($L1$) and the super-harmonic lock-in ($L2$) in Fig. 5.9.

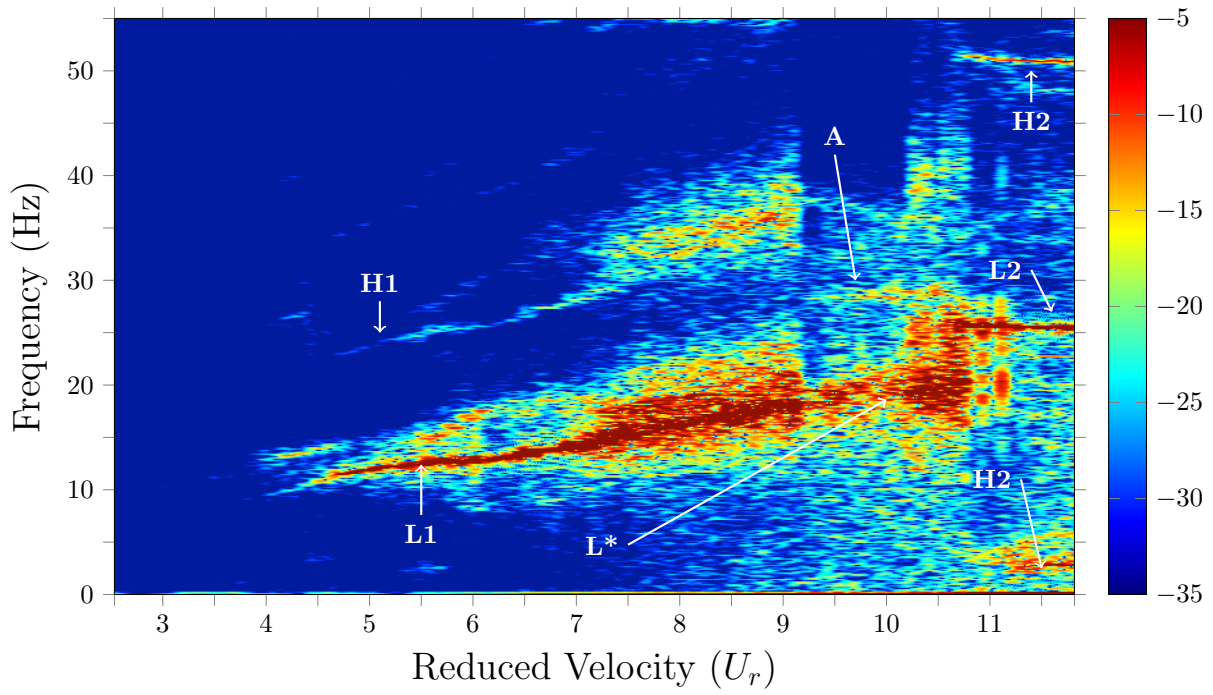

(a)

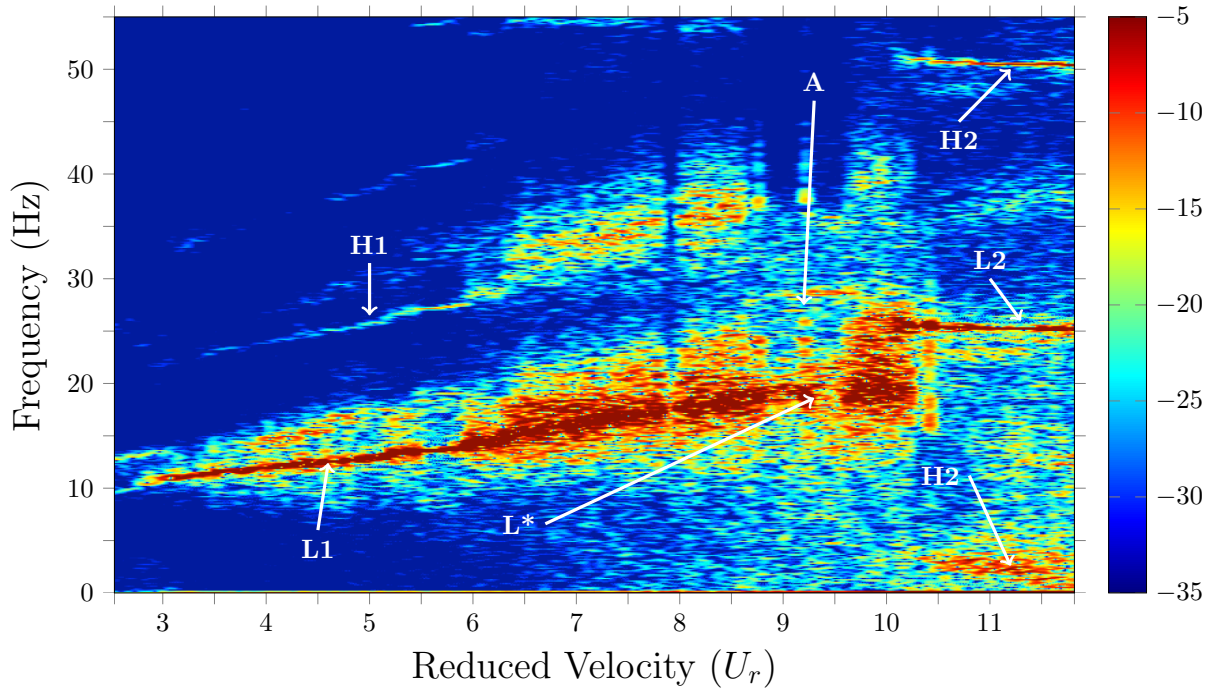

(b)

Figure 5.9. Spectrogram of the dynamic response collected at 1/3 span for both ramping conditions while (a) increasing and (b) decreasing the flow velocity across a U_r range of 2.53 to 11.82.

Chapter 6

Conclusion

In this work, a flexible cylinder with an $AR = 31$ and $m^* = 1.63$ undergoing VIV in uniform cross-flow is experimentally investigated. The testing is conducted using a high speed water tunnel and a displacement laser to collect the cylinder's transverse response at two separate span-wise locations. Several notable VIV phenomena were observed and detailed in this thesis, and the major findings are as follows.

(a) Lock-in between the vortex shedding frequency and cylinder's fundamental frequency is observed around $U_r = {}^1/_{St}$. Evidence of higher-order harmonic components is documented during the first lock-in resonance. (b) Multi-frequency excitation affects the VIV response at both high and low reduced velocities. (c) Asymmetric response dominates when the flow speed is between 0.95 and 1.2 ${}^m/_s$. (d) Lock-in at ${}^2/_3\times$ the first natural frequency is evident during the asymmetric response regime. (e) A lock-in at two times the fundamental natural frequency is also observed. In addition, both sub- and super- harmonics of the resonance frequency are evident in the frequency spectrum obtained from this lock-in period. (e) Data from trials in which the flow speed is either slowly increased or decreased indicate hysteresis.

6.1 Recommendation for Future Work

Due to the range of flow speeds tested, the results are limited to vortex shedding frequencies below 30 Hz, which only excite up to the first natural frequency of the cylinder. Further studies capturing the embedded cylinder's VIV response at higher flow speeds are recommended, such as investigating the cylinder's nonlinear behavior beyond the super-harmonic resonance lock-in. Regarding fine-tuning the experimental parameters, the discrepancies discussed in Section 3.1.3 should be addressed, including assembly of a new test article with a more uniform cross sectional area and more robust mounting conditions. Additionally, it is recommended that further experimentation focus on the the VIV response of an embedded flexible structure that is free to move both in the transverse and streamwise directions. Then, comparisons between the VIV behaviors could be distinguished with those of a cylinder constrained in a different degrees-of-freedom (DOF).

The quality of experiments can be improved by incorporating more instrumentation. For example, implementing an additional displacement laser would permit for simultaneous VIV response collection at different locations along the cylinder's span. This allows for more proper comparisons between the spatial variance of response amplitude and forcing frequency. Additionally, employing a particle image velocimetry (PIV) system would provide insight on the nature of the vortices formed during VIV. This would be beneficial for studying nonlinear phenomena such as response asymmetry and super-harmonic resonance lock-in.

Bibliography

[1] R. D. Belvins, *Flow-Induced Vibrations*. New York: Van Nostrand Reinhold Co., 1977.

[2] D. Lucor, J. Foo, and G. E. Karniadakis, "Vortex mode selection of a rigid cylinder subject to VIV at low mass-damping," *Journal of Fluids and Structures*, vol. 20, pp. 483–503, 2005.

[3] H. Curtis, "Operation and maintenance of a high-speed water tunnel," Master's thesis, University of Georgia, 2018.

[4] R. Bourguet, G. E. Karniadakis, and M. S. Triantafyllou, "On the validity of the independence principle applied to the vortex-induced vibrations of a flexible cylinder inclined at 60^o," *Journal of Fluids and Structures*, vol. 53, pp. 58–69, 2015.

[5] J. Werdigier, "Criticism is growing over shell's response to oil leak," *The New York Times*, 2011.

[6] X. Han, Y. Tang, Z. Feng, Z. Men, A. Qiu, W. Lin, and J. Wug, *Naval Engineering*, ch. Vortex-Induced Vibration of a Marine Riser: Numerical Simulation and Mechanism Understanding. License IntechOpen, 2018.

[7] F. J. Huera-Huarte and P. W. Bearman, "Wake structures and vortex-induced vibrations of a long flexible cylinder—part 1: Dynamic response," *Journal of Fluids and Structures*, vol. 25, pp. 969–990, 2009.

[8] B. Sanaati and N. Kato, "A study on the effects of axial stiffness and pre-tension on VIV dynamics of a flexible cylinder in uniform cross-flow," *Applied Ocean Research*, vol. 27, pp. 198–210, 2012.

[9] H. Zhu, P. Lin, and J. Yao, "An experimental investigation of vortex-induced vibration of a curved flexible pipe in shear flows," *Ocean Engineering*, vol. 121, pp. 62–75, 2016.

[10] Q. Han, Y. Ma, W. Xu, Y. Lu, and A. Cheng, "Dynamic characteristics of an inclined flexible cylinder undergoing vortex-induced vibrations," *Journal of Sound and Vibration*, vol. 394, pp. 306–320, 2017.

[11] W. Chen, Q. Zhang, H. Li, and H. Hu, "An experimental investigation on vortex-induced vibration of a flexible inclined cable under a shear flow," *Journal of Fluids and Structures*, vol. 54, pp. 297–311, 2015.

[12] H. Lie and K. E. Kaasen, "Modal analysis of measurements from a large-scale VIV model test of a riser in linearly sheared flow," *Journal of Fluids and Structures*, vol. 22, pp. 905–917, 2006.

[13] A. D. Trim, H. Braaten, H. Lie, and M. A. Tognarelli, "Experimental investigation of vortex-induced vibration of long marine risers," *Journal of Fluids and Structures*, vol. 21, pp. 335–361, 2005.

[14] Y. Gao, S. Fu, J. Wang, L. Song, and Y. Chen, "Experimental study of the effects of surface roughness on the vortex-induced vibration response of a flexible cylinder," *Ocean Engineering*, vol. 103, pp. 40–54, 2015.

[15] H. Zimmer, "Modal excitation of a flexible cylinder undergoing vortex induced vibrations," Master's thesis, University of Rhode Island, 2014.

[16] J. Song, L. Lu, B. Teng, H. Park, G. Tang, and H. Wu, "Laboratory tests of vortex-induced vibrations of a long flexible riser pipe subjected to uniform flow," *Ocean Engineering*, vol. 38, pp. 1308–1322, 2011.

[17] Y. Ma, W. Xu, T. Pang, Q. Wang, and J. Lai, "Dynamic characteristics of a slender flexible cylinder excited by concomitant vortex-induced vibration and time-varying axial tension," *Journal of Sound and Vibrations*, vol. 485, p. 115524, 2020.

[18] E. D. Gedikli and J. M. Dahl, "Mode excitation hysteresis of a flexible cylinder undergoing vortex-induced vibrations," *Journal of Fluids and Structures*, vol. 69, pp. 308–322, 2017.

[19] H. Cen, R. Carriveau, and D. S. K. Ting, "Effects of mass ratio on hydrodynamic response of a flexible cylinder," *Journal of Marine Science and Application*, vol. 15, pp. 50–62, 2016.

[20] J. K. Vandiver, "Dimensionless parameters important to the prediction of vortex-induced vibrations of a long, flexible cylinder in ocean currents," *Journal of Fluids and Structures*, vol. 7, pp. 423–455, 1993.

[21] T. Sarpkaya, "A critical review of the intrinsic nature of vortex-induced vibrations," *Journal of Fluids and Structures*, vol. 19, pp. 389–447, 2004.

[22] M. P. Païdoussis, S. J. Price, and E. de Langre, *Fluid-structure Interactions: Cross-Flow-Induced Instabilities*. New York: Cambridge University Press, 2010.

[23] A. Khalak and C. H. K. Williamson, "Motions, force, and mode transitions in vortex-induced vibrations at low mass-damping," *Journal of Fluids and Structures*, vol. 13, pp. 813–851, 1999.

[24] F. J. Huera-Huarte, P. W. Bearman, and J. R. Chaplin, "On the force distribution along the axis of a flexible circular cylinder undergoing multi-mode vortex-induced vibrations," *Journal of Fluids and Structures*, vol. 22, pp. 897–903, 2006.

[25] L. Lee and D. Allen, "Vibration frequency and lock-in bandwidth of tensioned, flexible cylinders experiencing vortex shedding," *Journal of Fluids and Structures*, vol. 26, pp. 602–610, 2010.

[26] G. Riches and C. Morton, "Wake dynamics in the lower branch and desynchronization regions of 1DOF VIV," *International Symposium on Turbulence and Shear Flow Phenomena*, 2019.

[27] F. J. Huera-Huerta, Z. A. Bangash, and L. M. González, "Towing tank experiments on the vortex-induced vibrations of low mass ratio long flexible cylinders," *Journal of Fluids and Structures*, vol. 48, pp. 81–92, 2014.

[28] X. Wu, F. Ge, and Y. Hong, "A review of recent studies on vortex-induced vibrations of long slender cylinders," *Journal of Sound and Vibrations*, vol. 28, pp. 292 –308, 2012.

[29] J. Dahl, *Vortex-Induced Vibration of a Circular Cylinder with Combined In-line and Cross-flow Motion*. PhD thesis, Massachusetts institute of Technology, 2008.

[30] A. Modir, M. Kahrom, and A. Farshidianfar, "Mass ratio effect on vortex induced vibration of a flexibly mounted circular cylinder, an experimental study," *International Journal of Marine Energy*, vol. 16, pp. 1–11, 2016.

[31] H. Zhu, P. Lin, and J. Yao, "Vortex-induced vibration and mode transition of a curved flexible free-hanging cylinder in exponential shear flows," *Journal of Fluids and Structures*, vol. 84, pp. 56–76, 2018.

[32] Y. Modarres-Sadeghi, M. P. Päıdoussis, C. Semler, and E. Grinevich, "Experiments on vertical slender flexible cylinders clamped at both ends and subjected to axial flow," *Philosophical Transactions of the Royal Society a-Mathematical Physical & Engineering Sciences*, vol. 366, pp. 1275–1296, 2008.

[33] J. K. Vandiver, V. Jaiswal, and V. Jhingran, "Insights on vortex-induced, traveling waves on long risers," *Journal of Fluids and Structures*, vol. 25, pp. 641–653, 2009.

[34] J. V. Ulveseter, M. J. Thorsen, S. Sævik, and C. M. Larsen, "Simulating fundamental and higher harmonic VIV of slender structures," *Applied Ocean Research*, vol. 90, p. 101856, 2019.

[35] J. Wu, D. Yin, H. Lie, C. M. Larsen, R. Baarholm, and S. Liapis, "On the significance of the higher order stress in riser VIV response," *Journal of Offshore Mechanics and Arctic Engineering*, vol. 141, p. 011705, 2018.

[36] T. K. Prasanth, V. Premchandran, and S. Mittal, "Hysteresis in vortex-induced vibrations: critical blockage and effect of m^*," *Journal of Fluid Mechanics*, vol. 671, pp. 207–225, 2011.

[37] R. H. J. Wilden and J. M. R. Grahamn, "Three distinct response regimes for the transverse vortex-induced vibrations of circular cylinders at low reynolds numbers," *Journal of Fluids and Structures*, vol. 22, pp. 885–895, 2006.

[38] S. Baek, S. B. Lee, and H. J. Sung, "Response of a circular cylinder wake to superharmonic excitation," *Journal of Fluid Mechanics*, vol. 442, pp. 67–88, 2001.